AN INVESTIGATION OF SOLAR CHIMNEY POWER PLANT CONCEPT AND ITS APPLICABILITY FOR DIFFERENT U.S. CLIMATE ZONES

A Thesis

by

YOUSEF M ALMARZOOQ

Submitted to the office of Graduate and Professional Studies of
Texas A&M University
in Partial fulfillment of the requirement for the degree of

MASTER OF SCIENCE

Chair of Committee,	Michael Pate
Committee Members,	Dion S. Antao
	Pavel V. Tsvetkov
Head of Department,	Andreas A. Polycarpou

December 2019

Major Subject: Mechanical Engineering

ABSTRACT

The Solar Chimney Power Plant (SCPP) concept was modeled, analyzed and applied to different locations (climate zones) throughout the U.S. The SCPP system includes three main components, namely the collector, the chimney and the turbine, with the horizontal collector covering a large area at ground level, the vertical chimney located at the center of the collector and the turbine mounted at the bottom of the chimney. The SCPP functions by heating air that gains momentum due to buoyancy forces that in turn rotate turbine blades producing mechanical work. As a result, the SCPP concept works under two basic principles, namely the greenhouse effect, and as noted above, the chimney effect. With regards to the greenhouse effect, the air enters the collector where it is heated by the sun's rays that strike the horizontal collector surface, which has a glazing cover that admits short-wave radiation while keeping the long-wave radiation emitted from the heated ground inside the collector.

A CFD model was formulated to investigate the behavior and performance of the SCPP concept with a particular focus on determining the maximum air velocity as a function of environmental conditions, namely incident solar radiation and outdoor ambient temperature. The power output from the SCPP was modeled analytically by using energy equations and heat transfer relationships that included solar radiation along with velocity inputs from the CFD model. The analytical model output was then used to develop a prediction model, based on a polynomial equation, for calculating generated power as a function of the Global Horizontal Irradiance (GHI) and the ambient temperature (T_∞) with both being dependent on geographical location and time of the year. To aid the application of the power prediction model to the real world, two more models, consisting of polynomial equations, were developed for calculating the GHI and T_∞ for different U.S climate zones and for varying times of the year. Afterwards, the annual power output for each climate zone was found, which will provide guidance for those that are considering the use of a SCPP system as an alternative to fossil fuel power plants.

ACKNOWLEGDEMENTS

First of all, I would like to thank my God for guiding me throughout my whole life. Second, I would like to thank my advisor, Dr. Michael Pate, for supporting and helping me throughout my graduate studies and research. Also, I would like to thank Dr. Dion and Dr. Tsvetkov for offering their support and being in my committee.

Special thanks to my great mother and to my lovely wife for their uncountable support and prayers.

CONTRIBUTORS AND FUNDS SOURCES

Contributors

This work was supported by a thesis committee consisting of Dr. Michael Pate [chair] and Dr. Dion S. Antao [member] of the J. Mike Walker ’66 Department of Mechanical Engineering and Dr. Pavel V. Tsvetkov [member] of the Department of Nuclear Engineering.

Funding Sources

Graduate study was supported by Saudi Arabian Cultural Mission (SACM).

NOMENCLATURE

A	Area (m^2)
h_∞	Convective heat transfer coefficient ($W/m^2.K$)
ρ	Density (kg/m^3)
μ	Dynamic viscosity (Pa.s)
η	Efficiency
ε	Emissivity
E	Energy
h	Enthalpy (kJ/kg)
F	Force (N)
GHI	Global Horizontal Irradiance (W/m^2)
g	Gravitational acceleration (m/s^2)
E_G	Ground emissive power (W/m^2)
α_s	Ground solar absorptivity
q"	Heat flux (W/m^2)
$\dot{m}$	Mass flow rate (kg/s)
$\dot{P}$	Power (W)
P	Pressure (Pa)
G_s"	Solar irradiance (W/m^2)
$\dot{Q}_s$	Solar Power (W)
c_p	Specific heat (J/kg.K)
σ	Stefan-Boltzmann constant ($W/m^2.K^4$)
T	Temperature (K)
α	Thermal diffusivity (m^2/s)
β	Thermal expansion coefficient (1/K)
t	Time
v	Velocity (m/s)

TABLE OF CONTENTS

LIST OF FIGURES

LIST OF TABLES

1. INTRODUCTION AND LITRATURE REVIEW

1.1 Introduction

Since the start of humanity, energy has been and will continue to be one of the most important needs for mankind, whether fire from the first centuries to the rockets and satellites that we are sending to space today. Furthermore, day by day our dependency on energy increases. For example, 20 years ago cell phones were not as common as they are today, so there was no interest in carrying a charger with you, while today this has become an essential life style. Similarly, the heating and cooling both residential and commercial buildings has become an extreme necessity. In summary, our need for electricity continuously increases, even though the conventional methods used for electricity production have proven to be harmful to the environment. In addition, conventional energy sources will not always be available. For example, oil will be depleted one day, and the same can be said for other natural resources that are not renewable.

Lately, there has been an increased movement toward “renewable energy”, which is any energy source that does not deplete, such as solar energy, wind energy, tidal energy...etc. Moreover, solar energy is one of the most promising kinds of renewable energy since solar power production techniques are so many, with one of them being called the solar chimney power plant (SCPP), which is the focus of this study.

The solar chimney, also called the solar updraft tower, is a renewable energy power plant that produces energy by using solar heating. The solar chimney produces energy by using two basic concepts, the greenhouse effect and the buoyancy effect. Furthermore, the solar chimney power plant (SCPP) consists of three main parts, the collector, the chimney (or the tower) and the turbine. The collector is basically a glazing cover that covers the area surrounding the tower and

admits the short-wave solar rays, while keeping the long-wave radiation from the heated ground under the collector cover, which means that the greenhouse effect is taking place in the collector. Moreover, the tower, which is located in the collector's center, is simply a long tube that helps to updraft the heated air flow, and as a result, the chimney effect takes place. To summarize, the collector captures the solar energy and the tower works as a chimney to produce an air movement within its perimeter, so that a turbine can be mounted in the flow to convert kinetic energy to mechanical energy. Finally, an electrical generator that is coupled to the turbine converts the mechanical energy to electrical energy. Figure 1-1 provides an overview of a basic solar chimney power plant, including aforementioned components and effects.

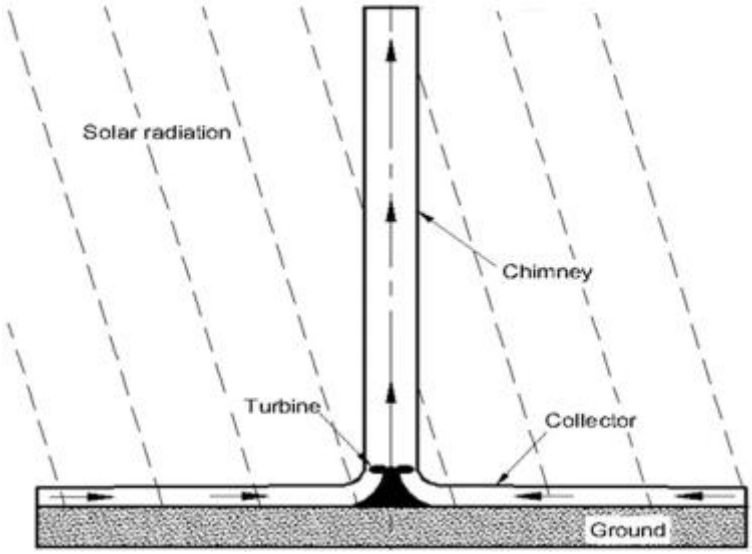

Figure 1-1 Schematic of Solar Chimney Power Plant. Reprinted from Najm and Shaaban 2018

In this study the concept of a SCPP system will be investigated both numerically and analytically, and then its performance will be evaluated on a monthly and annual basis for different climate zones in the United States.

The climate zones of the United States can be classified based on two parameters, namely the temperature and the humidity. For instance, the U.S climate zones are named 1A, 2A, 2B …etc, with the numbers representing the temperature and the letters representing the humidity. The temperature ranges from very hot (1) to very cold (7), while the humidity has only three categories, namely humid (A), dry (B) and marine (C). In this study, the SCPP is assumed to operate in all of the U.S climate zones, which total 18 climate zones, based on zone 3 being further divided into several subzones. To aid acquits of SCPP and weather data, each zone is represented by a different city as presented in Table 1-1

Table 1-1 U.S Climate Zones Included in this Study

Climate Zone	City, State	Climate Zone	City, State	Climate Zone	City, State
1A	Miami, FL	3B-W	El Paso, TX	4C	Seattle, WA
2A	Houston, TX	3B-LV	Las Vegas, NV	5A	Chicago, IL
2B	Phoenix, AZ	3B-N	Sacramento, CA	5B	Denver, CO
3A-W	Dallas, TX	3C	Santa Monica, CA	6A	St. Paul, MN
3A-E	Montgomery, AL	4A	Washington DC	6B	Cheyenne, WY
3B-E	Lubbock, TX	4B	Amarillo, TX	7A	Fargo, ND

Specifically, the SCPP concept will be applied to each climate zone in order to evaluate the capacity of each climate zone for power generation so as to identify not only the best location for SCPP operations but also the potential economic viability for each climate zone.

1.2 Literature Review

One of the first attempts to adopt the solar chimney concept was by Cabanyes (Cabanyes 1903), who had the goal of heating a house. However, the first prototype of a solar power plant based on the solar chimney was built in Manzanares, Spain (Haaf et al. 1983, 3-20). This Spanish prototype was planned to be used for only three years, but it produced energy for seven years, which proved both the reliability and viability of solar chimney power plants. Based on modeling and experiments the peak power output of the Spanish prototype was about 50 kW, with the physical dimensions of the prototype being provided in Table 1-2 . These dimensions are especially important because they were also used in the SCPP study reported herein.

Table 1-2 Spanish Prototype Parameters (Haaf et al. 1983, 3-20)

Parameter	Value
Tower height	194 m
Tower diameter	10 m
Collector diameter	244 m
Collector area	46,000 m^2
Collector height	1.8 m

Since the construction and modeling of the Spanish prototype, investigations and studies of solar chimney power plants have increased, most likely prompted by this prototype having been built, operated and then modeled and validated with real world data. Specifically, since 2016, a number of investigations have been carried out in different parts of the world, with these efforts being a combination of developing numerical models and building/operating experimental prototypes.

Hu (Hu, Leung, and Chan 2017) numerically investigated the impact of the chimney's geometry, including the divergent chimney concept, on the output power of a SCPP. The investigation included the effects of several parameters such as, the chimney entrance to exit-area ratio (AR), the divergent angle (DA) of the chimney wall and the size of the system. This study revealed a parabolic behavior in the performance of the SCPP as the AR and DA are increased.

In addition to the above, Shirvan (Milani Shirvan et al. 2017, 350-360) performed a case study on a Zanjan prototype solar-chimney power plant that included a numerical investigation and sensitivity analysis of the parameter effects on maximum power output. These parameters were collector-roof height and inclination, along with chimney diameter and height. The research results showed that as the chimney height and diameter increases then the potential maximum-power output increases. On the other hand, increasing the collector-roof height reduces the potential maximum-power output.

Huang (Huang et al. 2017, 100-106) conducted a two-dimensional simulation by using a new solar radiation model for the collector. Huang's new solar model is basically a two-parallel plate model where radiation heat transfer occurs between them. In addition to the proposed 2-D model, Huang proposed three more models, including an energy storage model, an air flow and heat

transfer model, and a turbine model. A numerical simulation of the Manzanares plant, which was mentioned earlier, produced results similar to the experimental data from the literature.

Ayadi (Ayadi et al. 2018, 649-662) conducted experimental and numerical investigations on the effects of the collector height on the solar-chimney performance, with a good agreement being shown between the numerical and the experimental results. Ayadi's investigation showed that collector heights have a noticeable effect on generated power, with the generated power increaseing as the collector height decreases.

Rabehi (Rabehi et al. 2018, 1093-1101) numerically simulated a solar chimney power plant by utilizing a fan model. Rabehi's research results showed that solar radiation has an obvious impact on the flow and heat transfer characteristics of a SCPP, while turbine pressure drop has only a slight effect on collector efficiency, and a noticeable impact on power output.

Hassan (Hassan, Ali, and Waqas 2018, 411-425) used a numerical analysis to study the effects of varying the slope of the collector and the diverging angle of the chimney, and it was found that air temperature and velocity increase with increasing the collector slope. However, the effect of increasing the collector slope has a limit since higher collector slopes can disturb the smoothness of the airflow by forming vortices and recirculation in the air, which can in turn reduce the overall performance of the SCPP.

Building on these previous investigations found in the literature and described above, the study reported herein formulated a CFD model of a SCPP, and then it is used to develop a solar model of the SCPP, based on simplified algebraic equations that can be used to calculate SCPP performance as a function of solar radiation and outdoor temperature. Finally, the validated simplified model is used to investigate the feasibility of the SCPP concept for different U.S

climate zones, which are characterized by monthly average radiation levels and monthly average outdoor temperature over a one-year period.

1.3 Research Objective and Scope of Work

In this research a CFD analysis will be performed on a solar chimney power plant with the goal of determining and optimizing system performance in order to apply the concept of solar chimney power plant to different climate zones in the United States over a typical one-year period.

The major tasks to achieve the project objectives are as follow:

1. Perform a literature review in order to find and evaluate solar chimney concepts from a historical standpoint, while at the same time focusing on the latest research from 2016 onward, including CFD analysis papers.
2. Select an existing SCPP model concept and solar model and then develop an improved CFD analysis model, by expanding and upgrading the exciting model.
3. After building, validating and upgrading the existing SCPP and solar model, the final CFD-based SCPP system model will be used to formulate algebraic equations for determining SCPP system performance as a function of solar radiation levels and outdoor temperature for a specified geometry.
4. Select eighteen different cities spread throughout the U.S, with each city represented by one of 18 different climate zones, in order to check the feasibility of applying the SCPP concept to different geographical locations. Weather data equations are formulated for each climate zone from measured solar radiation and ambient temperature so that

monthly average solar radiation values and monthly average outdoor temperature can be found.

Using these environmental parameters equations, the SCPP system is applied to 18 different climate zones in the U.S. in order to check the feasibility of monthly and annual energy output for different geographic locations.

5. After performing the above desired investigations and formulating the aforementioned algebraic equations, a comparison of SCPP performance for different locations in the U.S will be performed in order to build an understanding of how the SCPP concept can be adopted within the United States and to determine the economic viability of future applications.

2. CFD MODELING OF SCPP SYSTEM

2.1 Introduction

Computational Fluid Dynamics (CFD) is the numerical study of fluid mechanics, and powerful CFD codes, such as ANSYS (ANSYS-FLUENT), provide quick and accurate simulation results of real-life engineering problems and applications. Moreover, a CFD analysis can save time and money when modeling and analyzing systems in that various geometries and sizes can be easily analyzed, without time-consuming and costly constructions. (Şahin and Acir 2015, 22-25)

The 19.2 version of ANSYS will be used in this research for creating the CAD model of the SCPP and for performing the CFD analysis of system operations.

2.2 Governing Equations

In this study, the three governing equations, namely conservation of mass, momentum and energy will be solved simultaneously by the CFD code (i.e. FLUENT).

The conservation of mass is expressed in Equation 2.1:

$$\frac{\partial \rho}{\partial t} + \nabla \cdot (\rho \vec{v}) = 0 \qquad 2.1$$

where ρ, t, and $\vec{v}$ are density, time and velocity vectors, respectively.

Next, the conservation of momentum in FLUENT is expressed as:

$$\frac{\partial}{\partial t}(\rho \vec{v}) + \nabla \cdot (\rho \vec{v} \vec{v}) = -\nabla p + \nabla \cdot (\bar{\bar{\tau}}) + \rho \vec{g} + \vec{F} \qquad 2.2$$

where,

$$\bar{\bar{\tau}} = \mu\left[(\nabla\vec{v} + \nabla\vec{v}^T) - \frac{3}{2}\nabla\cdot\vec{v}I\right] \quad 2.3$$

Equation 2.2 represents the general form of the momentum equation, where p, $\bar{\bar{\tau}}$ and $\rho\vec{g}$ are the static pressure, the stress tensor and the gravitational body force, respectively. In Equation 2.3, μ and I are the molecular viscosity and the unit tensor, respectively.

The last equation is the energy equation, and it is expressed as:

$$\frac{\partial}{\partial t}(\rho E) + \nabla\cdot\left(\vec{v}(\rho E + p)\right) = \nabla\cdot k_{eff}\nabla T + \nabla\cdot(\bar{\bar{\tau}}_{eff}\cdot\vec{v}) + S_h \quad 2.4$$

where, k_{eff} is the effective conductivity, and S_h is any source of heat other than conduction and viscous dissipation, which are represented by the first two terms in the right hand side of Equation 2.4.

The term E in the left hand side of Equation 2.4 is expressed as:

$$E = h - \frac{p}{\rho} + \frac{v^2}{2} \quad 2.5$$

where h is the enthalpy of the fluid and defined as follows:

$$h = \int_{T_{ref}}^{T} c_p dT$$

where T_{ref} is 298 K, and c_p is the specific heat.

In this study, several assumptions have been made in order to simplify these equations of motion. One of the most important assumptions for capturing the buoyancy effect is the Boussinesq model. The Boussinesq model is the appropriate model for the solar chimney power plant concept since it assumes that the air density is a function of the temperature only, which is important in this study because the driving force inside the SCPP system is the density difference

between the ambient air and the air inside of the system. Furthermore, the Boussinesq model is represented by the thermal expansion coefficient β, which can be expressed as:

$$\beta = -\frac{1}{\rho}(\frac{\partial \rho}{\partial T})_p \quad 2.6$$

The effect of the temperature on the density can be seen in Equation 2.6. However, since the temperature difference in the SCPP system is small (i.e., 20 K), the density can be represented as:

$$(\rho - \rho_0) = -\rho_0 \, \beta (T - T_0) \quad 2.7$$

The Boussinesq model in FLUENT uses Equation 2.7 for calculating the density that is associated with the buoyancy force in the momentum equation, while ρ_0 will be used in the continuity equation, energy equation and the left hand side of the momentum equation.

Another assumption that can simplify the above equations of motion is to assume an incompressible flow. This assumption will simplify the mass equation to:

$$\nabla \cdot \vec{v} = 0 \quad 2.8$$

Also, the stress tensor will be affected by the incompressible assumption, and Equation 2.3 becomes:

$$\bar{\bar{\tau}} = \mu \nabla \vec{v} \quad 2.9$$

All assumptions mentioned coupled with the fact that the energy source term (S_h) is not necessarily needed in each thermodynamics case, the energy equation will be simplified by canceling the viscous heating term and the energy source term. Moreover, applying the above assumptions will affect the momentum equation as well. So, after applying the above assumptions and dividing the momentum equation by ρ_0, Equations 2.4 and 2.2 become:

$$\frac{\partial \vec{v}}{\partial t} + \vec{v}\nabla \cdot \vec{v} = -\frac{1}{\rho_0}\nabla p + \frac{\mu}{\rho_0}\nabla^2 \vec{v} + \vec{g}[1 - \beta(T - T_0] \quad (2.10)$$

$$\frac{\partial T}{\partial t} + \vec{v} \cdot \nabla T = \alpha \nabla^2 T \quad (2.11)$$

where α is the thermal diffusivity, which is expressed as:

$$\alpha = \frac{k}{\rho c_p}$$

2.3 CFD Modeling of The Spanish Prototype

A 2-D CAD model was created with the aid of the design modeler, which is a CAD software within ANSYS, by using the same dimensions as the Spanish prototype, as shown in Figure 2-1. Moreover, the boundary conditions used herein are similar to those used by Xu (Xu et al. 2011, 876-883) with some modifications. The seven different boundary conditions used in this study are presented in Table 2-1, which also includes boundary values, and they are inlet, ground, collector (the transparent roof), bend (the transition region between the collector and the chimney), chimney, axis (axis of symmetry used for axisymmetric approach), and outlet. In addition, the meshing tool contained in ANSYS is used to generate the mesh, with the element size being 0.11m, the total number of elements being 125664, and the number of nodes being 128599. Furthermore, a 2-D approach is used for the CFD model of the SCPP.

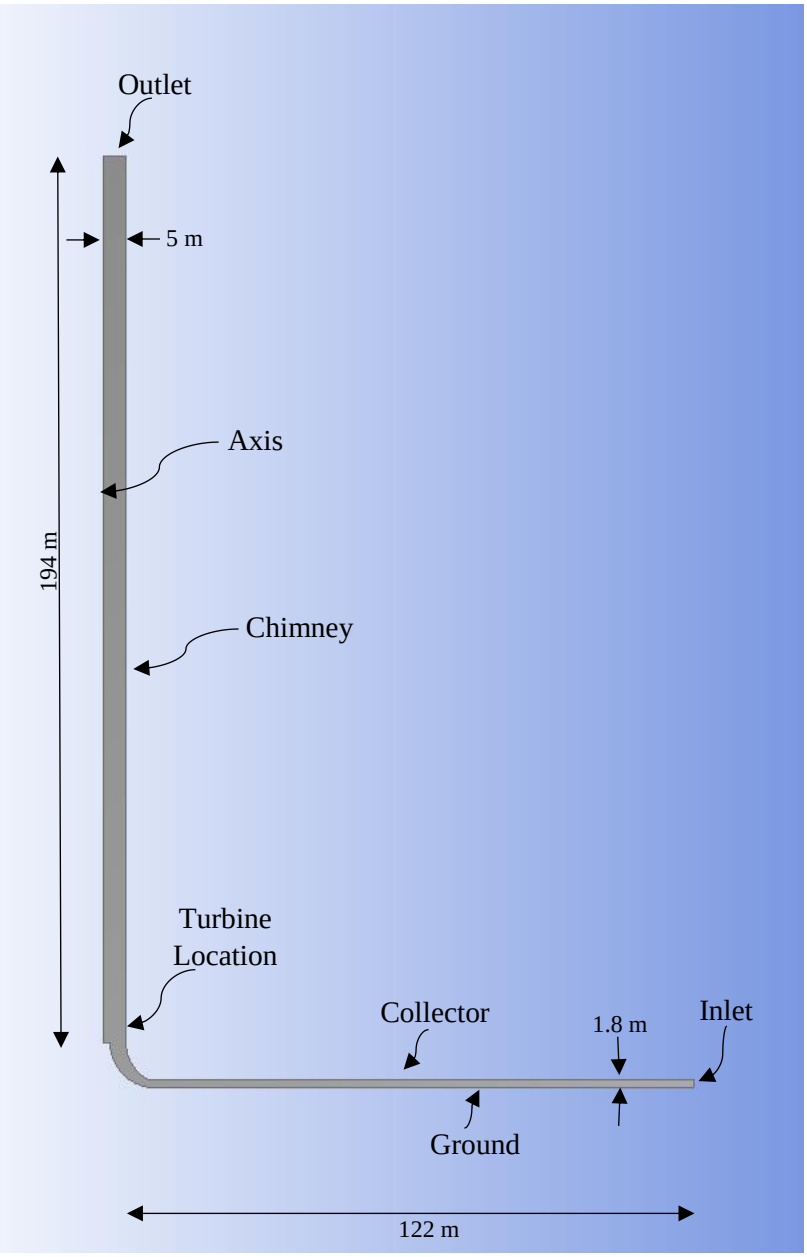

Figure 2-1 CAD Model of the Spanish Prototype

Table 2-1 Boundary Condition for the CFD Model

Place	Type	Value
Collector Inlet	Pressure Inlet	P_i = 0 Pa (gage)
Ground	Heat Flux	500 W/m^2
Collector	Wall	T= 293 K/h =1 0 W/m^2
Chimney	Wall	0 W/m^2 (Insulated)
Chimney Outlet	Pressure Outlet	P_o = 0 Pa (gage)
Axis	Axis	N/A

After the CAD model was meshed, FLUENT was used to perform the CFD analysis. First, the CAD model was imported to FLUENT, and the report quality was generated, which ensured that the mesh quality was within a reasonable range. Then, under the 'General' option on 'setup' in FLUENT, the solver was chosen to be a pressure-based type, steady, and axisymmetric. Also, the gravity was defined during this step.

Next, under the 'model' option on the 'setup', the energy equation was turned on, and the turbulent model chosen was the realizable k-epsilon model (Stockinger 2016). The air properties were then defined under 'materials' for different temperature ranges. Moreover, the operating conditions, such as operating temperature and pressure, could be modified easily under the 'cell zone conditions' option. The boundary conditions are defined after that, under the 'Boundary Conditions' option.

After finishing the setup stage, the solution stage was addressed, which required certain procedures before running the calculation. First, under 'Solution' there is an option called 'Method', which is used to specify the solution method. The pressure-velocity coupling scheme was chosen here, and the spatial discretization was specified. Afterwards, the residual absolute criteria could be identified under the 'Monitors' icon, with the absolute criteria in this study

being 10^{-6}. Next, the initialization process was initiated and the calculation step was ready to be started. Lastly, under the 'Run Calculation' option, the number of the desired iterations were defined, enabling the simulation to begin.

The above simulation in ANSYS, was then used to get the desired result by selecting the 'Result' icon in FLUENT, which in this study was to find the values of the velocity at specified locations throughout the air-flow region.

2.4 Solar Radiation Modeling

An important step in the modeling effort is to model the solar radiation admitted by the collector in a solar chimney power plant, which can be a challenge in that there are different approaches, based on different assumptions, which can be used for modeling the solar radiation. One approach is to model the solar radiation by applying an equivalence heat flux as the ground boundary condition, which is one of six boundary conditions mentioned in Table 2-1, while then transferring energy to the air by using a convection boundary condition. The first step in deriving the model is to apply an energy balance to a control surface near the ground as illustrated in Figure 2-2.

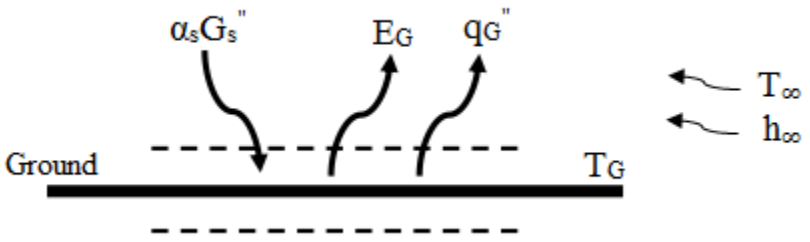

Figure 2-2 Energy Balance at the Ground under the Collector

Assuming that energy absorbed by the ground is equal to the energy out of ground results in:

$$\dot{E}_{in} = \dot{E}_{out} \tag{2.12}$$

or,

$$\dot{E}_{in} - \dot{E}_{out} = 0 \tag{2.13}$$

and as a result,

$$\alpha_s G_s" - E_G - q_G" = 0 \tag{2.14}$$

where,

α_s: Ground Absorptivity

$G_s"$: Solar irradiance (W/m^2)

E_G: Ground Emissive Power (W/m^2)

$q_G"$: Ground Heat Transfer by Convection (W/m^2)

Moreover,

$$E_G = \varepsilon_G \sigma {T_G}^4 \tag{2.15}$$

$$q_G" = h_\infty (T_G - T_\infty) \tag{2.16}$$

where,

ε_G: Ground Emissivity

σ: Stefan-Boltzmann Constant (5.67*10^{-8} W/m^2.K^4)

T_G: Ground Temperature (K)

h_∞: Convection Heat Transfer Coefficient (W/m^2.K)

T_∞: Ambient Temperature (K)

Combining terms, Equation 2.14 becomes:

$$\alpha_s G_s" - \varepsilon_G \sigma {T_G}^4 - h_\infty (T_G - T_\infty) = 0 \qquad 2.17$$

So that Equation 2.17 contains different factors that affect the hot air under the collector, which eventually flows to the chimney to drive the turbine. Therefore, appropriate assumptions must be made in order to develop an accurate solar model of the solar rays hitting the collector. The ground absorptivity α_s and emissivity ε_G are assumed to be 0.95 and 0.575, respectively (Incropera and others 2007), while the convection heat transfer coefficient is assumed to be 10 W/m^2 (Xu et al. 2011, 876-883). All three of the above parameters are assumed to be constant throughout this study.

Now, every term in Equation 2.17 is assumed to be known except the ground temperature T_G; therefore, for a known solar irradiance $G_s"$, ambient temperature T_∞, ground absorptivity α_s, ground emissivity ε_G, and coefficient of convection h_∞, the ground temperature can be calculated by using Equation 2.17.

The above solar radiation model is used to calculate the ground temperature and the ground heat flux $q_G" = h_\infty (T_G - T_\infty)$, and then it is used in FLUENT as equivalent to the solar net energy entering the collector. In closing, there will be different ground heat flux values associated with each combination of solar irradiance $G_s"$ and ambient temperature T_∞ with typical values shown in Table 2-2, based on α_s= 095, ε_G= 0575 and h_∞= 10 W/m^2. As a result, the ground heat flux boundary condition associated with each combination of solar irradiance and ambient temperature is defined.

Table 2-2 Ground Temperature and Heat Flux Variation with Different G_s" and T_∞ Values

Solar Irradiance (W/m^2)	**Ambient Temperature (˚F)**	**Ambient Temperature (K)**	**Ground Temperature (K)**	**Ground Heat Flux BC q_G" (W/m^2)**
300	20	266.5	276.1	95.7
300	40	277.6	284.7	70.9
300	60	288.7	293.1	44.3
300	80	299.8	301.4	15.9
400	20	266.5	283.4	169.6
400	40	277.6	291.9	143.2
400	60	288.7	300.2	115.1
400	80	299.8	308.3	85.3
400	100	310.9	316.3	53.7
600	20	266.5	297.8	313.5
600	40	277.6	306.0	284.1
600	60	288.7	314.0	253.0
600	80	299.8	321.8	220.2
600	100	310.9	329.5	185.7
800	20	266.5	311.7	452.2
800	40	277.6	319.6	419.9
800	60	288.7	327.3	385.9
800	80	299.8	334.8	350.2
800	100	310.9	342.2	312.9
1000	20	266.5	325.1	585.9
1000	40	277.6	332.7	550.7
1000	60	288.7	340.1	513.9
1000	80	299.8	347.4	475.4
1000	100	310.9	354.5	435.3

2.5 Validation of CFD Model

In order to validate the previous CFD model, the experimental data from the Spanish prototype was compared to the simulation data in the present study. Moreover, the focus was in comparing the magnitude of the vertical velocity at the bottom of the chimney where the turbine is mounted. The comparison showed that the calculated theoretical vertical velocity was 7.3% above the

experimental value identified in the Spanish study. Specifically, the Spanish prototype reached a vertical velocity of 15 m/s when the solar radiation and ambient temperature were 1000 W/m^2 and 293 K, respectively (Haaf et al. 1983, 3-20). On the other hand, the CFD model in the present study results in a vertical velocity of 16.1 m/s after applying the ground heat flux approach, which produced an equivalence ground heat flux of 500 W/m^2 for the 1000 W/m^2 solar radiation and ambient temperature of 293 K after applying Equation 2.16.

2.6 CFD Results

After the previous validation of the CFD model, the Solar Chimney Power Plant model was then used to generate additional vertical velocity data for the same geometry and size of the Spanish prototype, which was tabulated and shown previously in Table 1-2 . Specifically, as mentioned earlier in Chapter one, the CFD model was used to generate data for a range of solar radiation and ambient temperature values, assuming that several other parameters are fixed at values found in the literature, with the results being tabulated in Table 2-3

Table 2-3 Corresponded Velocity for Different Global horizontal irradiance and Ambient Temperature

Global horizontal irradiance (W/m^2)	Ambient Temperature (˚F)	Ambient Temperature (K)	Ground Temperature (K)	Ground Heat Flux BC (W/m^2)	Film Temperature (K)	Velocity (m/s)
300	20	266.5	276.1	95.68	271.3	9.2
300	40	277.6	284.7	70.87	281.1	8.4
300	60	288.7	293.1	44.28	290.9	7.1
300	80	299.8	301.4	15.92	300.6	5.1
400	20	266.5	283.4	169.58	275.0	11.2
400	40	277.6	291.9	143.25	284.8	10.6
400	60	288.7	300.2	115.14	294.5	9.8
400	80	299.8	308.3	85.29	304.1	8.9
400	100	310.9	316.3	53.69	313.6	7.6
600	20	266.5	297.8	313.48	282.2	13.8

Table 2-3 Continued

Global horizontal irradiance (W/m^2)	Ambient Temperature (˚F)	Ambient Temperature (K)	Ground Temperature (K)	Ground Heat Flux BC (W/m^2)	Film Temperature (K)	Velocity (m/s)
600	60	288.7	314.0	253.03	301.4	12.8
600	80	299.8	321.8	220.21	310.8	12.2
600	100	310.9	329.5	185.71	320.2	11.5
800	20	266.5	311.7	452.23	289.1	15.6
800	40	277.6	319.6	419.91	298.6	15.2
800	60	288.7	327.3	385.88	308.0	14.8
800	80	299.8	334.8	350.19	317.3	14.3
800	100	310.9	342.2	312.86	326.6	13.7
1000	20	266.5	325.1	585.93	295.8	17.0
1000	40	277.6	332.7	550.72	305.1	16.7
1000	60	288.7	340.1	513.86	314.4	16.3
1000	80	299.8	347.4	475.38	323.6	15.8
1000	100	310.9	354.5	435.33	332.7	15.3

As shown in Table 2-3 , the desired output from the CFD model is the velocity upstream of the turbine at the bottom of the chimney, which is used in later chapters to calculate the power output from the SCPP. Moreover, it is obvious form Table 2-3 that the vertical velocity is affected by global horizontal irradiance and ambient temperatures, which are environmental conditions that vary with geographical location (or climate zones) and with the seasons (or time of year).

Figure 2-3 are color intensify plots showing vertical velocity at various locations near the bottom of the chimney as taken from the CFD model of the Spanish prototype, which was used to fix the size of the SCPP system in this study, but with different boundary conditions. It can be seen in the plot, that the maximum velocity take place at the bottom of the chimney.

Figure 2-3 Velocity Results from the CFD Model for GHI = 400 W/m^2, 600 W/m^2 and T_∞ = 40˚F, 60˚F

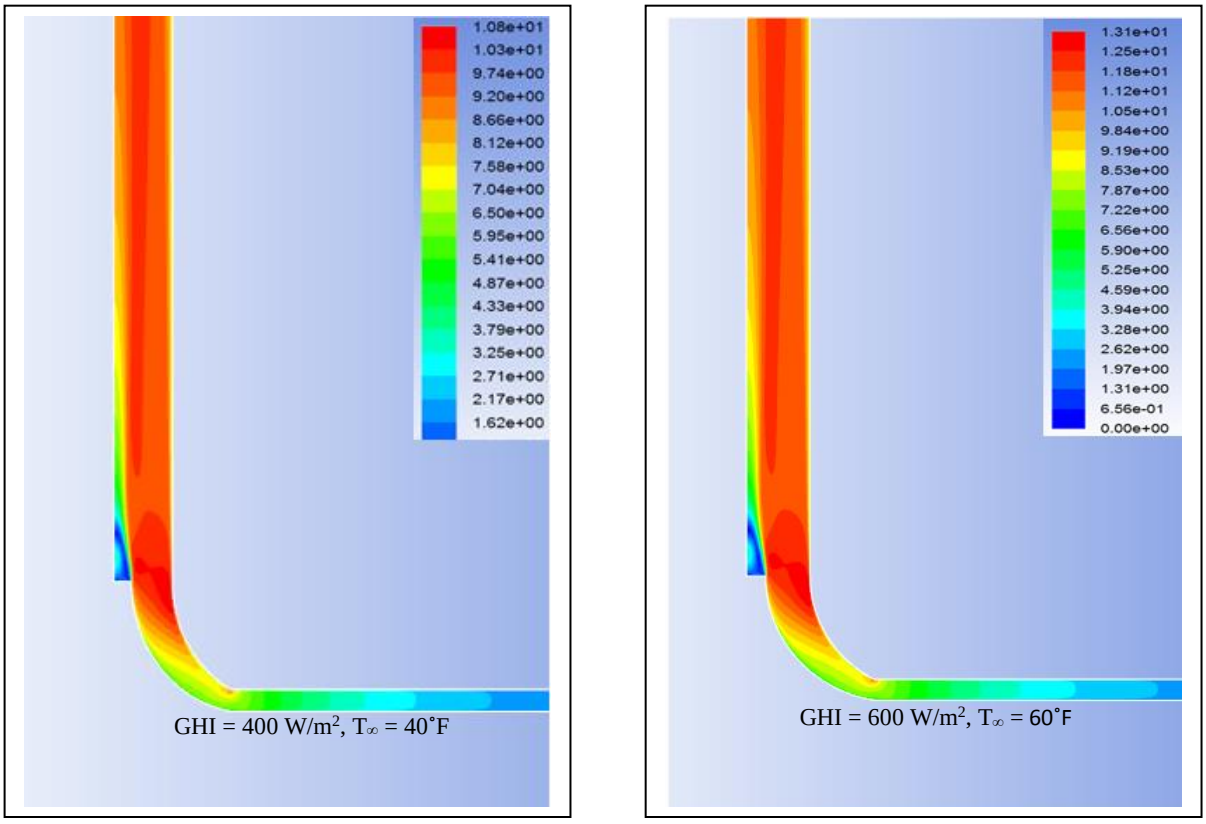

The results from Table 2-3 are plotted in Figure 2-4 to illustrate the behavior of air velocity for varying solar irradiances and ambient temperatures. It can be seen that the air velocity increases as the solar irradiance increases, while it decreases as the ambient temperature increases but to a lesser degree compared to that of solar irradiance.

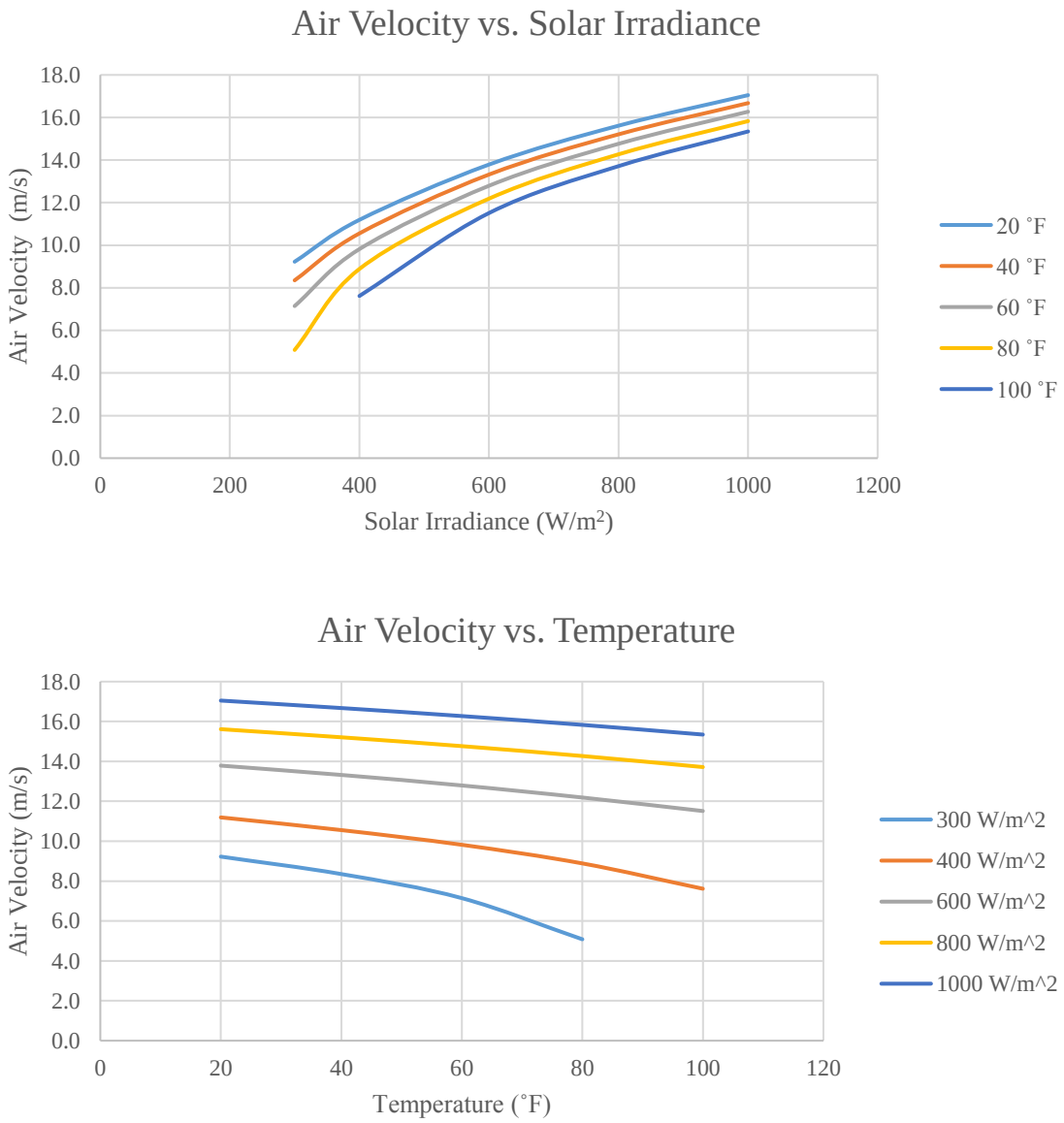

Figure 2-4 Air Velocity Behavior when Varying Solar Irradiance and Ambient Temperature

3. GLOBAL HORIZONTAL IRRADIANCE (GHI) CALCULATIONS

3.1 Introduction

Global Horizontal Irradiance (GHI) is the amount of solar energy received by a surface horizontal to the ground. As was discussed earlier, the airflow within the SCPP, and hence system performance, is affected by GHI and ambient temperature, which are in turn affected by location, including latitude, and time of year. Therefore, one of the major goals of this project is to evaluate SCPP performance for different U.S locations, represented by climate zones, over the period of a year. In this chapter, the method for getting the GHI for different climate zones from weather files will be explained, including the development of a third degree polynomials for calculating the GHI for different climate zones for any given month.

All of the data for GHI in this chapter were extracted from TMY3 (Typical Meteorological Year) data sets (NREL). TMY3 are environmental and climate data sets collected from 1961-1990 and 1990-2005 by the National Solar Radiation Data Base (NSRDB). Furthermore, TMY3 consists of average hourly data for 1020 locations in the United States, and one of these collected data sets is hourly GHI, which is important for this study.

3.2 Averaged GHI and Prediction Model

The development of a correlation for determining daily GHI is based on assuming that the behavior of the GHI value over the course of a day as the sun moves across the sky follows a sine wave for almost all locations. This assumption is based on observing that the value of GHI at the beginning of the day starts at a small value, and then it increases until reaching a maximum at solar noon in the middle of the day, followed by decreasing values until reaching zero at sunset. Though, the focus here will be on using the sine-wave assumption to calculate the hourly

GHI for each climate zone over the course of an average day that is assumed to occur at the middle (i.e. the 15th) of each of 12 months.

As mentioned, using TMY3 data sets, monthly average hourly GHI values for each climate zone, which are represented by one city for each climate zone, and for each month of the year were generated by using the sine wave assumption. However, monthly average hourly GHI determinations for each climate zone first require that the peak GHI (GHI_{Peak}) for the middle of each month determined, again by using TMY3 data sets for each climate zone. The GHI_{Peak} values for each month for each climate zone total 216=12X18 peak values, and they are tabulated in Table 3-1

Table 3-1 GHI_{peak} Values for Different Climate Zones over a Course of a Year

CZ	Month	Averaged GHI_{Peak} (W/m^2)	CZ	Month	Averaged GHI_{Peak} (W/m^2	CZ	Month	Averaged GHI_{Peak} (W/m^2
1A	January	554.4	**2A**	January	438.87	**2B**	January	549.03
	February	621.6		February	498.25		February	638
	March	698.8		March	597.74		March	714.19
	April	774.8		April	676.57		April	920.57
	May	732.8		May	692.9		May	971.81
	June	733.2		June	725.67		June	1001.43
	July	786		July	801.61		July	962.42
	August	720.1		August	691.1		August	947.19
	September	699.8		September	710.33		September	884
	October	618.8		October	631.13		October	721.1
	November	549.7		November	520.83		November	598.5
	December	534.1		December	425.87		December	488.16
3A-W	January	471.84	**3A-E**	January	449.06	**3B-E**	January	481.65
	February	538.39		February	550.64		February	571.82
	March	642.81		March	659.81		March	699.61
	April	773.03		April	784.13		April	850.6
	May	805.68		May	758.68		May	826.06
	June	872.93		June	753.77		June	878.13

Table 3-1 Continued

CZ	Month	Averaged GHI_{Peak} (W/m^2)	CZ	Month	Averaged GHI_{Peak} (W/m^2	CZ	Month	Averaged GHI_{Peak} (W/m^2
3A-W	July	867.48	**3A-E**	July	737.16	**3B-E**	July	825.16
	August	837.87		August	771.61		August	819.19
	September	730.57		September	718.87		September	700
	October	673.97		October	606.71		October	663.61
	November	495.97		November	508.77		November	508.03
	December	439.1		December	430.74		December	468.32
3B-W	January	546.65	**3B-LV**	January	474.65	**3B-N**	January	343.45
	February	678.64		February	599.82		February	455.57
	March	806.13		March	728.1		March	614.87
	April	952.23		April	893.47		April	715.67
	May	946		May	912.61		May	920.74
	June	988.2		June	966.7		June	934.27
	July	921.97		July	947		July	939.74
	August	864.29		August	939.13		August	882.65
	September	858.1		September	868.77		September	801.93
	October	679.94		October	684.55		October	622.19
	November	590.33		November	562		November	419.3
	December	523.52		December	483.48		December	306.35
3C	January	493.19	**4A**	January	326.74	**4B**	January	489.94
	February	513.61		February	398.89		February	562.21
	March	696.65		March	574.9		March	716.81
	April	849.67		April	706.33		April	802.87
	May	828.52		May	607.45		May	795.16
	June	920.17		June	733.7		June	879.43
	July	930.94		July	721.71		July	873.23
	August	913.65		August	721.68		August	820.97
	September	799.4		September	593.37		September	699.43
	October	590.06		October	555.03		October	682.74
	November	555.3		November	343.1		November	518.17
	December	445.16		December	322.29		December	463.13
4C	January	167.81	**5A**	January	305.9	**5B**	January	429.65
	February	337.43		February	395.18		February	518.93
	March	406.26		March	503.9		March	679.45
	April	560.33		April	548.53		April	639.9
	May	616.19		May	723.9		May	786.52
	June	606.07		June	709.1		June	893.23
	July	715.81		July	761.32		July	846.16
	August	635		August	647.61		August	829.81

Table 3-1 Continued

CZ	Month	Averaged GHI_{Peak} (W/m^2)	CZ	Month	Averaged GHI_{Peak} (W/m^2	CZ	Month	Averaged GHI_{Peak} (W/m^2
4C	September	560.5	**5A**	September	558.03	**5B**	September	725.5
	October	303.58		October	427.9		October	562.06
	November	158.1		November	319		November	406.4
	December	160.52		December	262.48		December	373.94
6A	January	265.97	**6B**	January	402.1	**7A**	January	275.19
	February	452.36		February	464.29		February	421.82
	March	370.68		March	629		March	507.23
	April	630.03		April	664.57		April	614.6
	May	581.97		May	730.87		May	697.06
	June	585.63		June	845.9		June	725.27
	July	615.61		July	800.81		July	697.52
	August	688.35		August	789.32		August	658.9
	September	569.77		September	643.57		September	557.97
	October	345.52		October	546.97		October	419.29
	November	247.27		November	417.3		November	315.9
	December	189.32		December	338.13		December	255.87

Inputting the values in Table 3-1 into the JMP statistics package, the following three degree polynomial was solved for GHI_{Peak} as a function of months (i.e. time of year) for any given climate zone:

$$GHI_{Peak} = C_1 + C_2M + C_3M^2 + C_4M^3 \quad 3.1$$

where,

C_1, C_2, C_3 and C_4: are the coefficients that represent each climate zone

M: Month

The above equation is made applicable to all climate zones by finding the unique values of the coefficients for each climate zone, with these values being tabulated in Table 3-2.

Table 3-2 GHI Prediction Model Coefficients

Climate Zone	C_1	C_2	C_3	C_4
1A	430.2626262	131.4495589	-14.97551845	0.3849391
2A	325.3273921	106.4626343	-4.3022705	-0.328841
2B	321.1715729	203.5712048	-15.4409895	-0.049239
3A-W	282.8190076	167.0638196	-11.3740765	-0.144973
3A-E	286.6022514	174.085294	-16.88094215	0.2769037
3B-E	245.4036679	231.266556	-25.31174015	0.6182077
3B-W	286.2407479	268.1072937	-30.9676921	0.8444678
3B-LV	229.9249079	238.4231565	-20.82079885	0.2034343
3B-N	76.9725995	236.7545806	-14.268894	-0.354868
3C	247.0484459	205.0741859	-16.14877875	0.0119425
4A	124.883658	195.302621	-17.004696	0.152208
4B	285.1950672	195.7309567	-18.5250518	0.2721924
4C	-70.42370652	238.9622496	-20.9375807	0.1714426
5A	78.58087273	205.3513081	-18.1123617	0.1603406
5B	241.8055676	173.0019843	-11.3685565	-0.216093
6A	138.7268961	143.2366583	-8.6645585	-0.273297
6B	198.5184973	181.9774425	-13.686217	-0.066994
7A	35.95024259	241.3993146	-24.85646455	0.5001269

To summarize, by specifying the location (i.e. climate zine) and the time of the year (i.e. the month), then the GHI_{Peak} can be found by using Equation 3.1 and the coefficients tabulated in Table 3-2. Furthermore, in a following section, each of the climate zones with their twelve different peak GHI values, representing each month of the year, can then be used to generate hourly GHI values for every single day of a specific month by applying a sine wave assumption.

3.3 Error Associated With the Prediction Model

In order to assess the error, the above polynomial was used to calculate the GHI_{Peak} for each month of all eighteen climate zones and then compared with the actual TMY3 values originally used to solve for climate zone coefficients. Table 3-3 presents a sample of this comparison for one specific climate zone, namely 3A-E, and for this specific case all but one of the values, which was the higher with a 6.8% error, had errors less than 5%. All of the peak GHI errors are plotted in Figure 3-1, and as can be seen the errors associated with this polynomial are nearly always less than 21%, and usually less than 4%. Also, R^2 values are always greater than 0.9.

Table 3-3 Comparison between Actual and Predicted GHI_{Peak} for Climate Zone 3A-E (Montgomery, AL)

Month	**Predicted GHI_{Peak} (W/m^2)**	**Actual GHI_{Peak} (W/m^2)**	**Error Percentage %**
January	444.08	449.06	1.1
February	569.46	550.64	-3.4
March	664.41	659.81	-0.7
April	730.57	784.13	6.8
May	769.62	758.68	-1.4
June	783.21	753.77	-3.9
July	773.01	737.16	-4.9
August	740.68	771.61	4.0
September	687.88	718.87	4.3
October	616.26	606.71	-1.6
November	527.51	508.77	-3.7
December	423.26	430.74	1.7

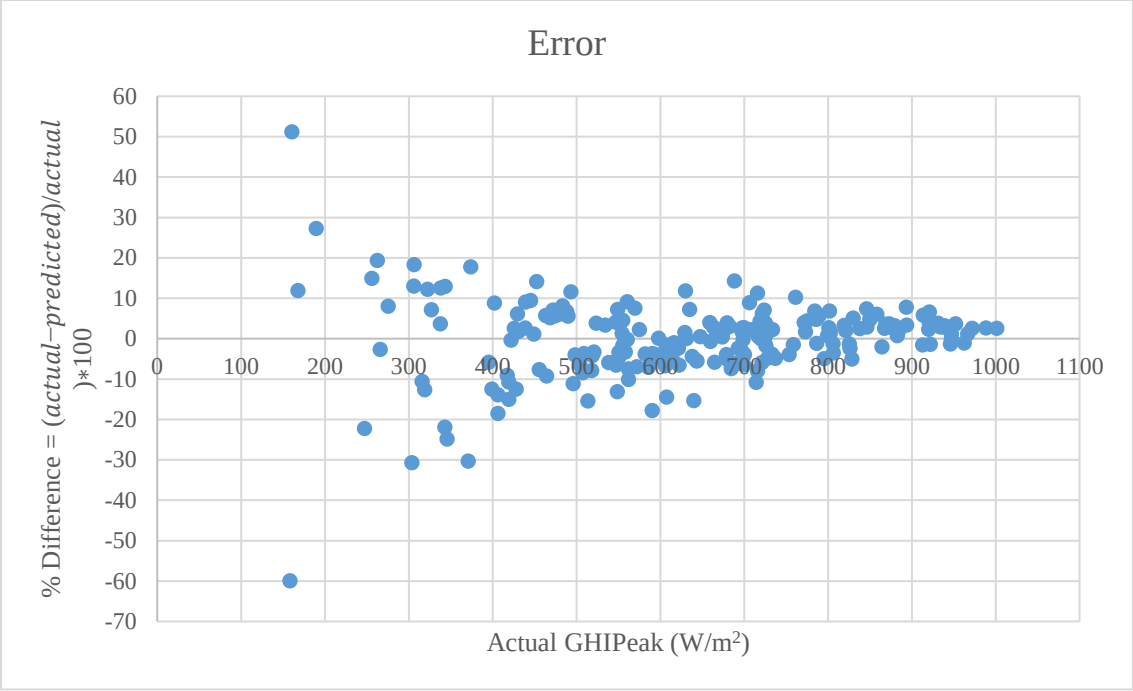

Figure 3-1 Difference Percentage between Actual and Predicted GHI_{Peak}

3.4 Sine Wave Assumption

As mentioned in Section 3.2, a sine wave assumption can be used to find the hourly GHI value for a representative day in the middle of each month (15th day) by using the known GHI_{Peak} values from the polynomial and by knowing the daylight length in hours. Specifically, GHI for any hour can be expressed as follow:

$$GHI_{Hourly} = GHI_{Peak}\, Sin(\frac{2\pi t}{\tau}) \qquad 3.2$$

where,

$\pi = 180°$

t: Time of Day (1st hour, 2nd hour …etc.)

$\tau = 2 * Length\ of\ the\ Day$

From Equation 3.2, it can be seen that the hourly GHI value is a function of the time and length of the day. Therefore, when the time-of-day, length-of-day and GHI_{Peak} values are defined with the latter being dependent on the month and climate zone, then the hourly GHI can be calculated. Of special importance, the GHI_{Hourly} parameter will later be used as solar radiation input to the SCPP model in order to calculate the power generated by a SCPP system.

Figure 3-2 provides a sample comparison between an actual GHI_{Hourly} curve computed from TMY3 data and a sine wave assumption curve for a specified location (CZ-1A) and at a certain time of the year (January). Moreover, the value of τ, which is two times the day length, in Equation 3.2 will vary with time of year and climate zone since the latitude varies for each climate zone.

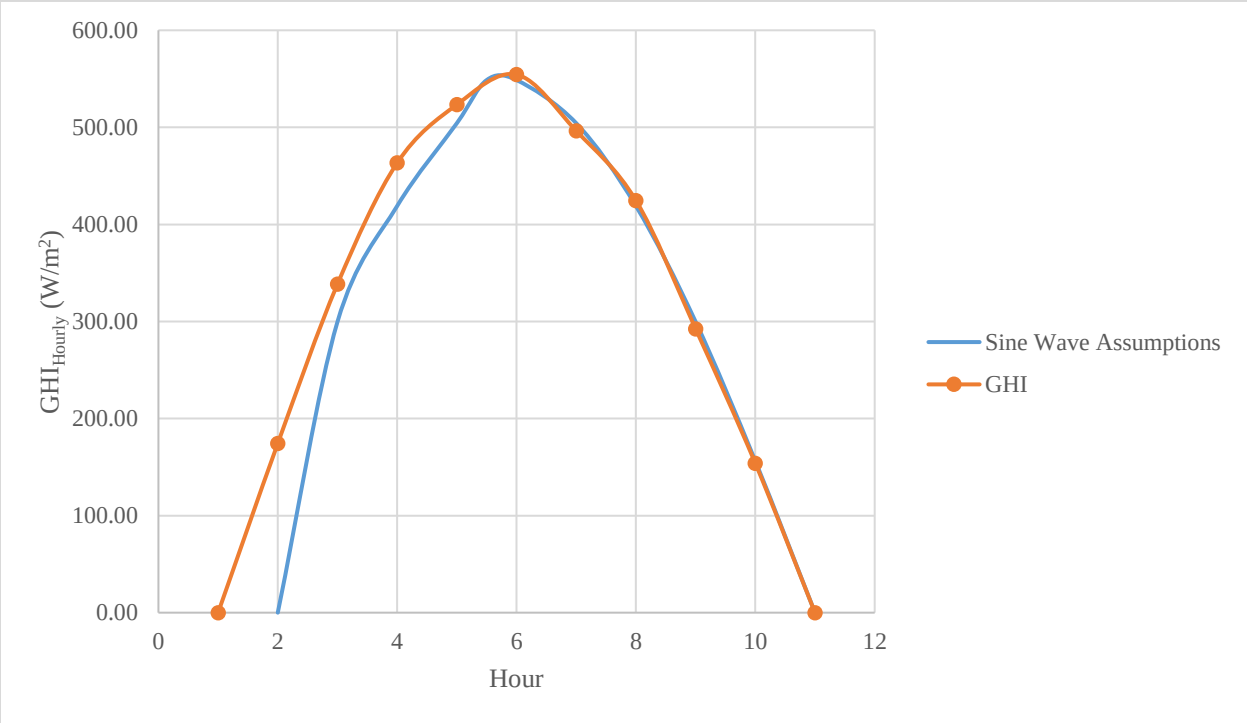

Figure 3-2 Comparison between Actual GHI_{Hourly} and Sine Wave Assumption for Climate Zone 1A at January 15th

3.5 Summary

The hourly GHI values for the 18 representative cities, which in turn represented 18 climate zones, were collected from TMY3 data sets and the monthly average GHI values were found. The peak values of GHI for each month were tabulated and coupled with the statistics package JMP so as to solve a third-degree polynomial, with coefficients being a function of climate zone. In addition, the error associated with this polynomial was assessed and found to be usually less than 4%. Furthermore, the sine wave assumption for calculating the hourly GHI values by knowing the peak GHI was introduced, and a sample comparison between the actual and sine wave assumption was illustrated, with the difference being minor.

4. AMBIENT TEMPERATURE (T_∞) CALCULATIONS

4.1 Introduction

A correlation for calculating the average ambient temperature for different U.S climate zones on a monthly basis is developed in this chapter. The approach used is similar to the procedures followed in the previous chapter for calculating the average peak GHI for each month for each climate zone. Again, the ambient temperature is important for calculating the output power of a SCPP as will be discussed in later chapters. The approach here differs from the Chapter 3 GHI approach in that rather than calculating and using an hourly temperature, only an average daily ambient temperature is calculated and used in the SCPP system model. This assumption is based on the fact that even though the temperature changes throughout the day, these changes are small compared to month-to-month and season-to-season changes, which are in fact accounted for. In contrast, hour-to-hour changes in GHI are necessary because solar radiation changes significantly throughout the day. A final point is that the SCPP power generated is affected more by solar radiation than it is by ambient temperature, as was shown earlier.

4.2 Averaged Ambient Temperature and Prediction Model

The monthly average daily temperature is calculated for each climate zone by averaging the highest and the lowest temperature of each month with values being taken from a website called Current Results (Osborn).

The average monthly temperature for each climate zone are tabulated in Table 4-1, and these values along with the statistics package JMP were used to generate a fourth-degree polynomial to predict the ambient temperature.

Table 4-1 Averaged Ambient Temperature Values for Different Climate Zones for a One Year Period

CZ	Month	Averaged Ambient Temperature (˚F)	CZ	Month	Averaged Ambient Temperature (˚F)	CZ	Month	Averaged Ambient Temperature (˚F)
1A	January	68	**2A**	January	53	**2B**	January	57.5
	February	70		February	56.5		February	60.5
	March	72.5		March	63		March	66
	April	75.5		April	69.5		April	73
	May	80		May	77		May	82
	June	83		June	82		June	90.5
	July	84		July	84.5		July	94.5
	August	84		August	85		August	93
	September	83		September	80		September	87.5
	October	80		October	71.5		October	76.5
	November	75		November	62.5		November	64
	December	70.5		December	54.5		December	56
3A-W	January	47	**3A-E**	January	46.5	**3B-E**	January	40
	February	51		February	50.5		February	44.5
	March	59		March	57.5		March	52
	April	66.5		April	64.5		April	60.5
	May	74.5		May	72.5		May	70
	June	82.5		June	79		June	77.5
	July	86.5		July	81.5		July	80.5
	August	86.5		August	81.5		August	79
	September	79		September	76		September	72
	October	68.5		October	65.5		October	61.5
	November	57.5		November	56.5		November	50
	December	48.5		December	48.5		December	40.5
3B-W	January	45.5	**3B-LV**	January	48.5	**3B-N**	January	46.5
	February	50		February	52.5		February	50.5
	March	56.5		March	59.5		March	54.5
	April	65		April	67		April	58.5
	May	74		May	77.5		May	65.5
	June	82		June	87		June	71.5
	July	83		July	92.5		July	75
	August	81		August	90.5		August	74.5
	September	75.5		September	82.5		September	71.5
	October	65		October	69.5		October	64
	November	53		November	56.5		November	53.5
	December	45		December	48		December	46

Table 4-1 Continued

CZ	Month	Averaged Ambient Temperature (˚F)	CZ	Month	Averaged Ambient Temperature (˚F)	CZ	Month	Averaged Ambient Temperature (˚F)
3C	January	57	**4A**	January	34.5	**4B**	January	37
	February	57		February	36		February	40
	March	57		March	44		March	47.5
	April	58.5		April	54		April	56.5
	May	60		May	64.5		May	66
	June	62.5		June	73		June	74.5
	July	65.5		July	77.5		July	78
	August	66.5		August	75		August	76.5
	September	67		September	68.5		September	69.5
	October	64.5		October	57.5		October	58.5
	November	60.5		November	46.5		November	46.5
	December	58		December	37		December	37
4C	January	42	**5A**	January	25	**5B**	January	31.5
	February	43.5		February	28.5		February	32.5
	March	46.5		March	38		March	40.5
	April	50		April	50		April	47.5
	May	56		May	61		May	57.5
	June	61		June	72		June	67
	July	66		July	76		July	74.5
	August	66		August	74		August	72.5
	September	61.5		September	66		September	63.5
	October	53		October	54.5		October	51.5
	November	45.5		November	41		November	38.5
	December	41		December	29.5		December	31.5
6A	January	16.5	**6B**	January	29	**7A**	January	9
	February	21.5		February	29.5		February	15
	March	33.5		March	35.5		March	27.5
	April	48		April	43		April	44.5
	May	60.5		May	52.5		May	57
	June	69.5		June	62		June	66
	July	74.5		July	69.5		July	71.5
	August	72		August	67.5		August	69
	September	63		September	58.5		September	59
	October	50		October	46.5		October	45.5
	November	34.5		November	35.5		November	28.5
	December	21		December	27.5		December	14

This aforementioned fourth-degree polynomial is a function of the time of the year (month), and it can be expressed as follow:

$$T_{\infty,monthly\ avg.} = B_1 + B_2M + B_3M^2 + B_4M^3 + B_5M^4 \qquad 4.1$$

where,

B_1, B_2, B_3, B_4 and B_5 :are the coefficients that represent each climate zone

M: Month

The five coefficients for each of 18 climate zones are tabulated in Table 4-2. As noted, the statistics package JMP along with the temperature data in Table 4-1 was used to solve for the 5 coefficients namely B_1 to B_5, for each climate zone.

Table 4-2 Ambient Temperature Prediction Model's Coefficients

Climate Zone	B_1	B_2	B_3	B_4	B_5
1A	70.334091	-3.49973	2.1100998	-0.241397	0.0075138
2A	56.972222	-8.828012	5.0845693	-0.614363	0.0208406
2B	67.030051	-17.54563	7.8495909	-0.910732	0.0308821
3A-W	50.987247	-14.30094	7.4738184	-0.895752	0.0306567
3A-E	50.406944	-12.26359	6.5955258	-0.800014	0.0277021
3B-E	51.304672	-15.68015	7.9961632	-0.971874	0.0341015
3B-W	54.848485	-13.20156	6.7328234	-0.803273	0.0273747
3B-LV	62.714646	-21.08289	9.5199713	-1.116364	0.0383523
3B-N	51.893308	-7.859343	4.2292219	-0.481199	0.0149676
3C	62.118434	-6.659085	2.6809016	-0.267017	0.0072152
4A	44.517424	-16.95194	8.5197327	-1.019948	0.0353052
4B	47.054924	-16.67257	8.2231443	-0.984238	0.0340308
4C	51.183965	-13.49192	5.6626356	-0.638535	0.0211294
5A	35.071717	-17.11692	8.9728972	-1.079018	0.0372232
5B	46.335354	-20.03664	8.9241866	-1.038164	0.0353919
6A	28.018434	-17.71013	9.5620831	-1.154701	0.0397574
6B	41.369167	-23.50252	10.182636	-1.18433	0.0407222
7A	18.735606	-16.11956	9.7272254	-1.203424	0.0418859

Therefore, the ambient temperature can be predicted by Equation 4.1 after defining the month and the geographical location. Unlike solar radiation, which was found on an hourly basis by using a sine wave approximation, there is no attempt herein to find hour-by-hour temperature rather the daily temperature is assumed to be constant and represented by the daily average temperature found from equation 4.1.

4.3 Error Associated with the Prediction Model

In order to assess the error, the above polynomial was used to calculate the predicted ambient temperatures (T_∞) for each month for all eighteen climate zones and then compared to the actual temperature values that were originally used to solve for the climate zone coefficients. Figure 4-1 represent the error between actual and predicted ambient temperature. As can be seen the resulting error associated with using this polynomial was always less than 8 ˚F, and usually less than 2 ˚F.

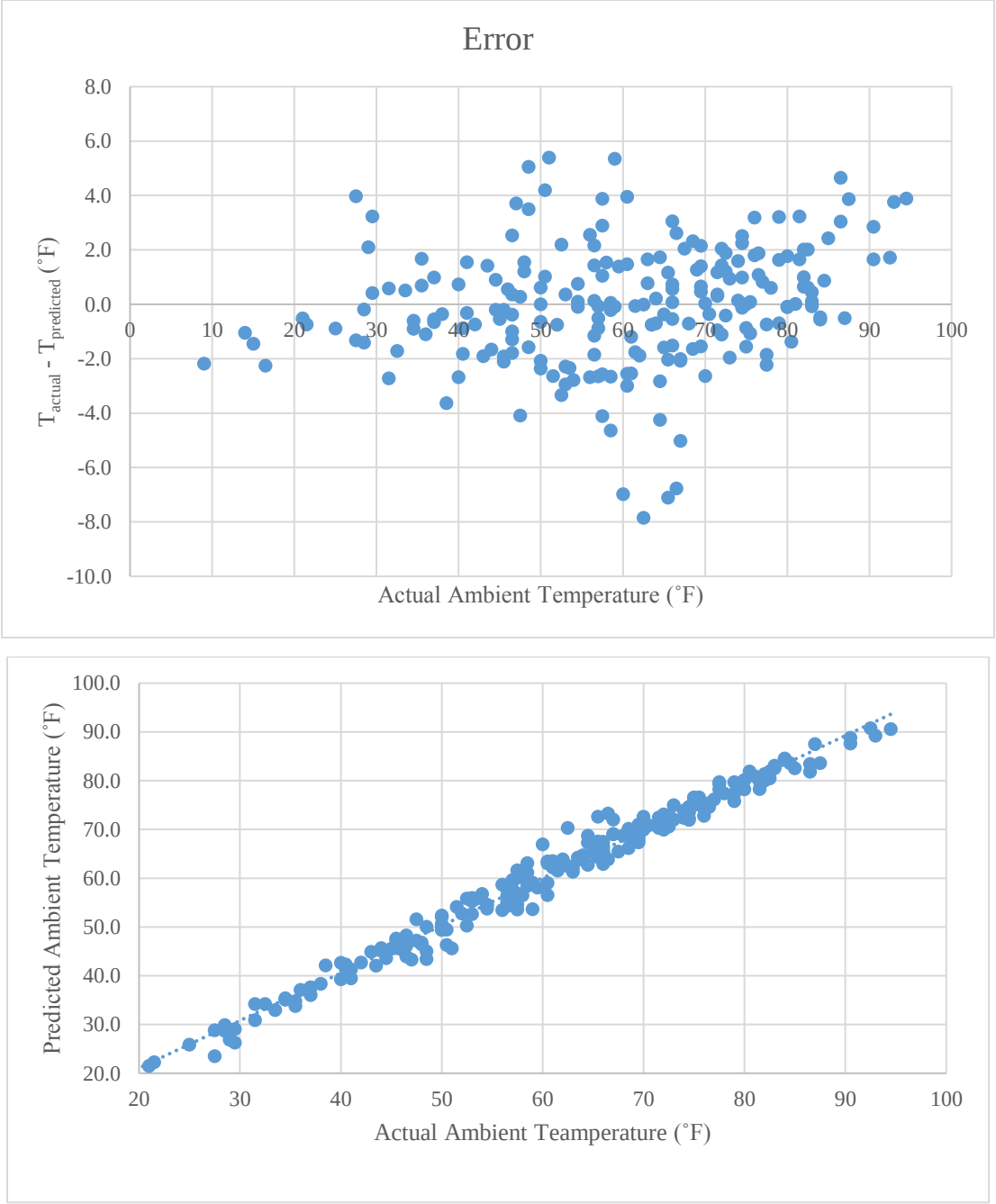

Figure 4-1 Error between Actual and Predicted Ambient Temperature

4.4 Summary

In summary, the monthly average temperature was determined for all different climate zones by averaging the lowest and highest temperature for a mid-month day (15^{th}), which is assumed to be representative of an average temperature for the month. Then, using this data a prediction model was created by using the statistics package JMP to determine coefficient values for each climate zone so that the monthly average temperature could be calculated as a function of month and location. This prediction model was then used to calculate the ambient temperature, which an important input parameter when the power production of the SCPP is later calculated and evaluated on an annual basis for each climate zone.

5. POWER GENERATION BY SCPP

5.1 Introduction

In the previous chapters, CFD techniques were applied to create a SCPP model with fixed geometry and size, which mirrored the Spanish prototype. In addition, two different models were developed for finding the two environmental parameters needed as inputs to the SCPP model, with one being the global horizontal irradiance (GHI) and other being the ambient temperature (T_∞). Chapter 5 will now present the development of an analytical model of an operating SCPP, which will then be the beginning of a prediction model for calculating the output power of a SCPP as a function of solar radiation and ambient temperature and the chimney velocity, which is the output of the aforementioned SCPP model.

The connection between the analytical model and the prediction model, with both developed in this chapter, is that the analytical model uses vertical velocities from the CFD model and energy balances to determine the SCPP power output for 5 sets of solar radiation and ambient temperatures, while the prediction model for output power is a working polynomial equation using the analytical model output. The output of the analytical model is a data file that consists of 25 (5X5) power outputs. As noted, the prediction model as a working equation, in a polynomial format, can be used to easily evaluate power outputs as a function of only two variables, namely solar radiation (GHI) and ambient temperature. In a later chapter, this prediction model equation will be coupled with solar radiation and ambient temperatures for each climate zone and for each month of the year to find SCPP power outputs both monthly and annually, throughout the U.S.

5.2 Output Power ($\dot{P}_{out}$) Analytical Model

According to Schlaich (Schlaich 1995), the output power from a SCPP is a function of three efficiencies, namely turbine, collector and tower, and the solar radiation contacting the collector as follows:

$$\dot{P} = \dot{Q}_s \, \eta_{turbine} \, \eta_{collector} \, \eta_{tower} \tag{5.1}$$

and,

$$\dot{Q}_s = G"_s A_{collector} \tag{5.2}$$

where,

The η variables: turbine, collector and tower efficiency

$\dot{Q}_s$: Solar Power gained by the collector (W)

$G"_s$: Solar Irradiance (W/m^2)

$A_{collector}$: Collector horizontal area (m^2)

In order to calculate the SCPP power output, all three of above efficiencies must be known either by assumption or by modeling. First, the value of the turbine efficiency is assumed to be the value specified by the turbine manufacturer. The collector and tower efficiencies require further investigations and modeling.

The efficiency of the collector is the fraction of the solar energy arriving at the outer collector surface ($\dot{Q}_s$) that then enters the collector ($\dot{Q}_{collector}$) so as to heat the inside air.

Thus,

$$\eta_{collector} = \frac{\dot{Q}_{collector}}{\dot{Q}_s} \quad 5.3$$

As noted, $\dot{Q}_{collector}$ can be treated as the energy gained by the air flowing below the transparent collector surface, and it can be determined by using the energy equation and the mass continuity equation as follows:

$$\dot{Q}_{collector} = \dot{m}\, c_p\, \Delta T \quad 5.4$$

and,

$$\dot{m} = \rho\, v\, A_{tower} \quad 5.5$$

where,

$\dot{Q}_s = GHI\, A_{collector}$

$\dot{m}$: Air mass flow rate (kg/s)

c_p: Air specific heat (kJ/kg.K)

ΔT: Temperature rise of air

ρ: Air density (kg/m^3)

v: Vertical velocity (m/s)

$A_{tower} = \pi\, r^2{}_{tower}$

By substituting Equations 5.2, 5.4 and 5.5 into Equation 5.3, the final form of the collector efficiency equation, $\eta_{collector}$, is:

$$\eta_{collector} = \frac{\rho\, v\, A_{tower} c_p\, \Delta T}{GHI\, A_{collector}} \quad 5.6$$

where,

$$A_{collector} = \pi\, r^2{}_{collector}$$

GHI: Global Horizontal Irradiance (W/m^2)

Next, the tower efficiency is basically the ratio between the air kinetic energy (KE) and the heat transfer at the bottom of the tower, and it can be expressed as follows:

$$\eta_{tower} = \frac{KE}{\dot{Q}_{tower}} \tag{5.7}$$

And,

$$KE = \frac{1}{2}\, \dot{m}\, v^2 \tag{5.8}$$

$$\dot{Q}_{tower} = \dot{m}\, c_p\, \Delta T \tag{5.9}$$

Substituting Equations 5.8 and 5.9 into equation 5.7 yields the tower efficiency as:

$$\eta_{tower} = \frac{v^2}{2\, c_p\, \Delta T} \tag{5.10}$$

The next step is to substitute equations 5.2, 5.6 and 5.10 into Equation 5.1, which is the power equation presented at the beginning of this chapter. The resulting power output equation is:

$$\dot{P} = \frac{1}{2}\, \rho\, \pi\, r^2{}_{tower}\, \eta_{turbine}\, v^3 \tag{5.11}$$

The vertical velocity, v, in equation 5.11 is the maximum vertical velocity without the turbine load (Schlaich 1995). However, in order to model the SCPP with the turbine load, Haaf (Haaf et al. 1983, 3-20) investigated and reported that for the Spanish prototype when the maximum power is reached, the vertical velocity across the turbine was equal to 8/10 of the maximum vertical velocity without the turbine model. As a result, Equation 5.11 can be corrected to get the power output of the SCPP with the turbine. So Equation 5.11 becomes,

$$\dot{P} = \frac{1}{2}\,\rho\,\pi\,r^2{}_{tower}\,\eta_{turbine}\,(0.8\,v)^3 \qquad 5.12$$

The results of the velocity from the CFD model in chapter 2, specifically Table 2-3 , will be used here in equation 5.12 to calculate the SCPP power output.

5.3 Connection Between Output Power ($\dot{P}_{out}$) and the two Environmental Parameters

It was shown that the power output of a SCPP can be calculated from Equation 5.12 after knowing values for the different parameters such as air velocity, air density, turbine efficiency, and tower radius. However, an equally important question is how this power output is related to the environmental parameters of global horizontal irradiance and ambient temperature with the simple answer being that these environmental parameters effect vertical velocity, which in turn affects power output. The effect that the global horizontal irradiance and ambient temperature has on the vertical velocity at the bottom of the tower in a SCPP was a major goal of the CFD analysis discussed in Chapter 2, with Table 2-3 presenting the resulting velocities as a function of global horizontal irradiance and ambient temperature. Combining all of the above information to include inputting velocities from Table 2-3 into Equation 5.12, Table 5-1 can be created, which is a table of power outputs as a function of global horizontal irradiances and ambient temperatures. As a side note, a turbine efficiency of 60% is used in Equation 5.12.

Table 5-1 Power Output for Different Global horizontal irradiance and Ambient Temperature

Global horizontal irradiance (W/m^2)	Ground Temperature (K)	Ground Heat Flux BC (W/m^2)	Ambient Temperature (˚F)	Ambient Temperature (K)	Velocity (m/s)	Work Output (kW)
300	276.1	95.7	20	266.5	9.2	12.3
300	284.7	70.9	40	277.6	8.4	8.8
300	293.1	44.3	60	288.7	7.1	5.3
300	301.4	15.9	80	299.8	5.1	1.9
400	283.4	169.6	20	266.5	11.2	21.7
400	291.9	143.2	40	277.6	10.6	17.6
400	300.2	115.1	60	288.7	9.8	13.7
400	308.3	85.3	80	299.8	8.9	9.8
400	316.3	53.69	100	310.9	7.6	6.0
600	297.8	313.48	20	266.5	13.8	39.6
600	306.0	284.13	40	277.6	13.3	34.5
600	314.0	253.03	60	288.7	12.8	29.6
600	321.8	220.21	80	299.8	12.2	24.8
600	329.5	185.71	100	310.9	11.5	20.3
800	311.7	452.23	20	266.5	15.6	56.1
800	319.6	419.91	40	277.6	15.2	50.2
800	327.3	385.88	60	288.7	14.8	44.5
800	334.8	350.19	80	299.8	14.3	39.0
800	342.2	312.86	100	310.9	13.7	33.7
1000	325.1	585.93	20	266.5	17.0	71.3
1000	332.7	550.72	40	277.6	16.7	64.7
1000	340.1	513.86	60	288.7	16.3	58.4
1000	347.4	475.38	80	299.8	15.8	52.2
1000	354.5	435.33	100	310.9	15.3	46.3

A study of SCPP power as a function of the two environmental parameters, namely solar radiation and ambient temperature, provides important understanding of SCPP operations and the potential for real-world applications. Using Table 5-1 data, power output from a SCPP is plotted against GHI for a range of T_∞ values in Figure 5-1. While in Figure 5-2 power output is plotted

against ambient temperature for a range of GHI values. From these two graphs one can say that the output power of a typical SCPP is increasing as the GHI increases meaning higher solar radiation levels produces more power, which is expected. On the other hand, the temperature has an opposite effect on SCPP power output, in that it decreases the power output as temperature increases, it can also be seen on the two plots, especially Figure 5-2, that the effect of temperature on power is much weaker than GHI.

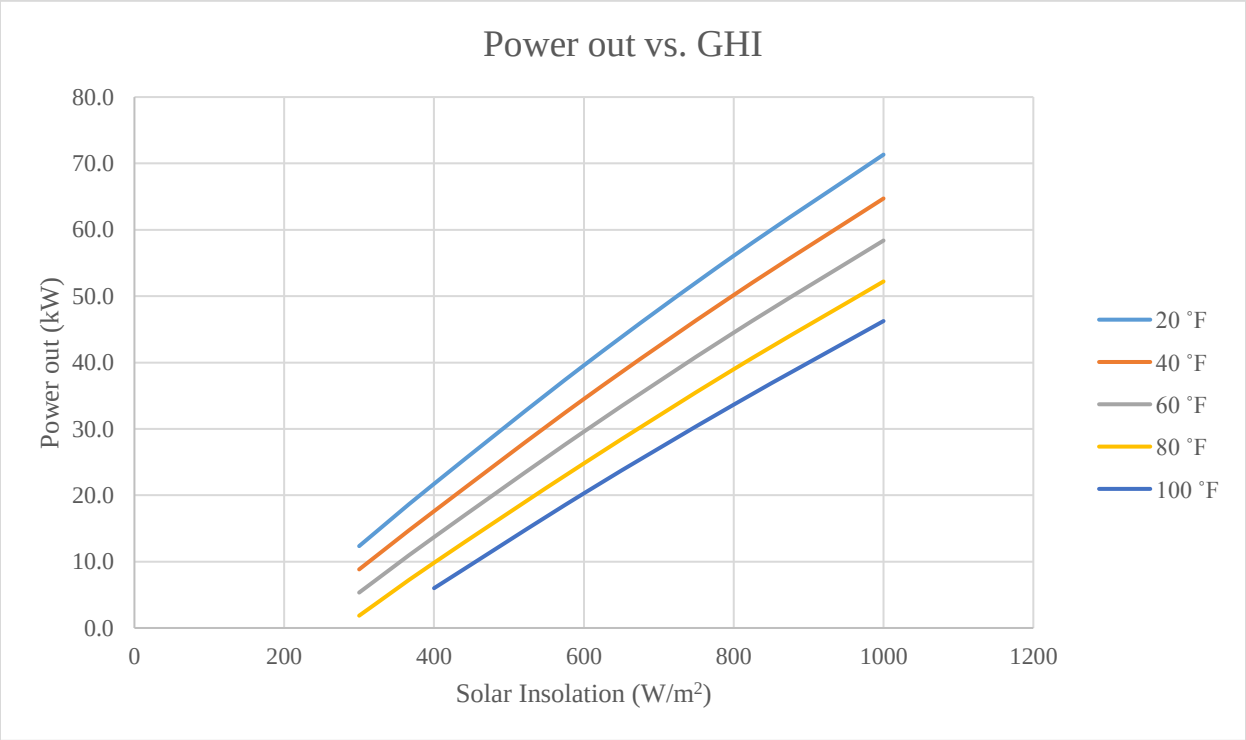

Figure 5-1 Power Output of a SCPP vs. GHI for Different T_∞ Values

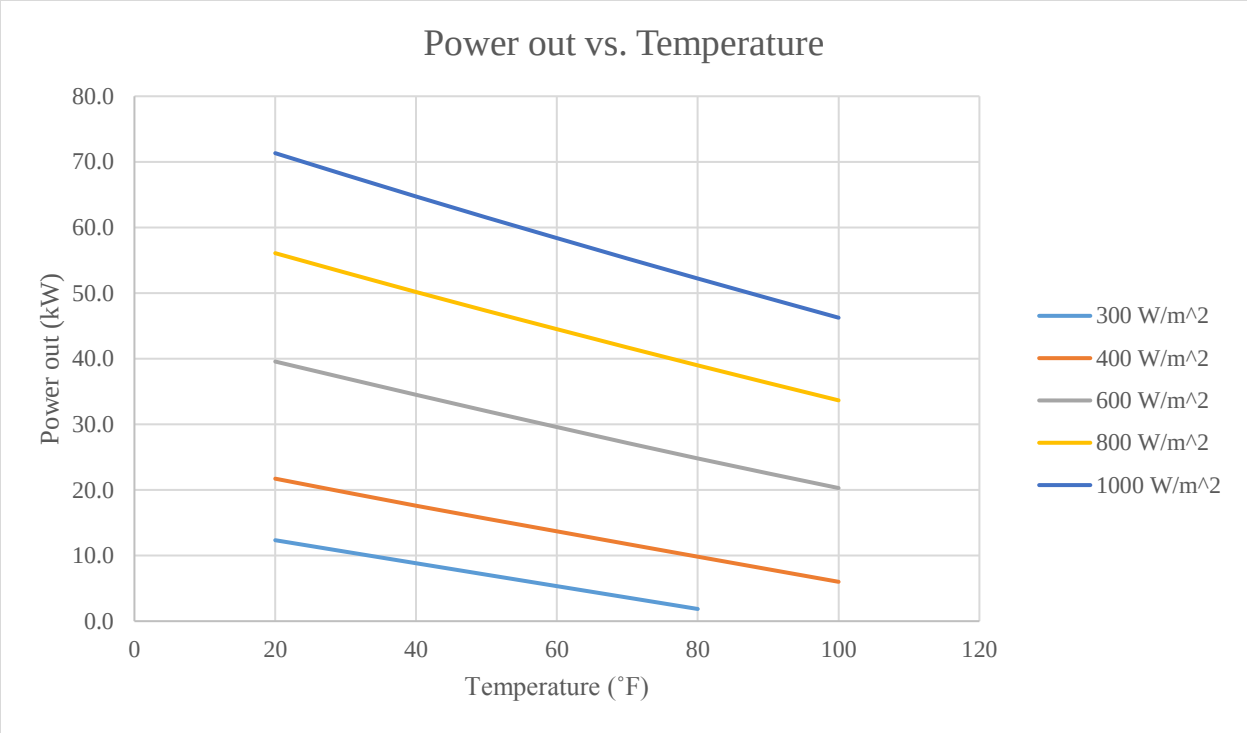

Figure 5-2 Power Output of a SCPP vs. T_∞ for Different GHI Values

5.4 Power Output Prediction Model

Similar to what was done previously for finding polynomial correlations for the two environmental parameters as a function of climate zones and time of year, a correlation for calculating the power output of a SCPP as a function of global horizontal irradiance and the ambient temperature was developed by using data tables and statistics package JMP. Specifically, values from Table 5-1 were taken into the statistics package JMP and Equation 5.13 was created as follows:

$$\dot{P}_{out} = C_1 + C_2 GHI + C_3 T_\infty + \{(T_\infty + C_4)(GHI + C_5)(C_6)\} \qquad 5.13$$

with the coefficients being:

C_1= -2.328230037 C_2= 0.0764493534 C_3= -0.242593138

C_4= -58.333333333 C_5= -633.33333333 C_6= -0.000209326

Combining the power equation polynomial and coefficient values results in the final working equation as follow:

$$\begin{aligned}\dot{P}_{out} = {} & -2.328230037 + (0.0764493534 * GHI) \\ & + (-0.242593138 * T_{\infty}) \\ & + \{(T_{\infty} - 58.333333333)(GHI \\ & - 633.33333333)(-0.000209326)\}\end{aligned} \quad 5.14$$

Thus, Equation 5.13 can be used to find the power output of a SCPP, with a geometry and size similar to the Spanish prototype, for any GHI and T_{∞} value that is within the range of values tabulated in Table 5-1 . Specifically, as with most correlations, Equation 5.13 has its own limits consistent with Table 5-1 , which is as follow:

for solar radiation, GHI (W/m^2)

$$300 < GHI\ (W/m^2) < 1000$$

and for ambient temperature, T_{∞} (˚F):

$$20 < T_{\infty}(°\text{F}) < 100$$

5.5 Error Associated with the Power Output Prediction Model

An investigation of the errors associated with using this power prediction model was performed by comparing the actual power output data from Table 5-1 which was used to originally develop the prediction correlation, with predicted power output values calculated by using equation 5.13. Table 5-2 provides this comparison in terms of tabulated percentage errors for all cases presented

in Table 5-1 while Figure 5-3 provides a plot of this error percentage as a function of actual power. As can be seen in both the table and plot, the error associated with the prediction model was always less than 15.5%, and usually less than 2%.

Table 5-2 Comparison between Actual and Predicted Output Power ($\dot{P}_{out}$)

GHI (W/m^2)	Ambient Temperature ($^{\circ}F$)	Actual Power (kW)	Predicted Power (kW)	Error Percentage %
300	20	12.3	13.1	-6.0
300	40	8.8	9.6	-9.0
300	60	5.3	6.2	-15.5
400	20	21.7	21.5	0.9
400	40	17.6	17.7	-0.3
400	60	13.7	13.8	-0.6
400	80	9.8	9.9	-0.8
400	100	6.0	6.0	-0.5
600	20	39.6	38.4	2.9
600	40	34.5	33.7	2.3
600	60	29.6	29.0	2.0
600	80	24.8	24.3	2.1
600	100	20.3	19.6	3.5
800	20	56.1	55.3	1.4
800	40	50.2	49.8	0.8
800	60	44.5	44.2	0.6
800	80	39.0	38.7	0.8
800	100	33.7	33.1	1.6
1000	20	71.3	72.2	-1.2
1000	40	64.7	65.8	-1.7
1000	60	58.4	59.4	-1.8
1000	80	52.2	53.1	-1.6
1000	100	46.3	46.7	-0.9

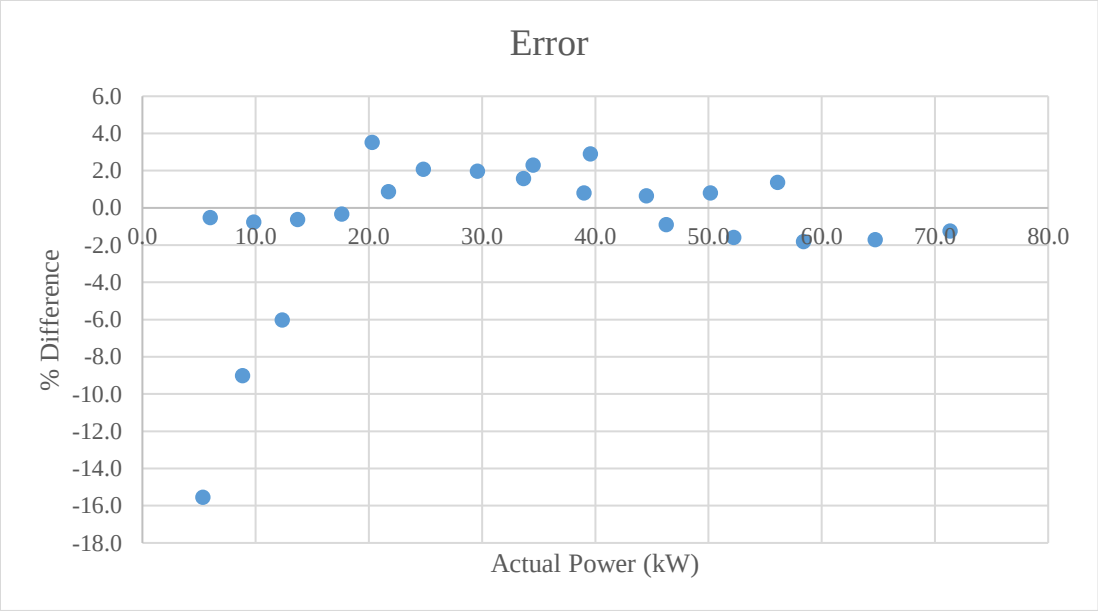

Figure 5-3 Difference Percentage between Actual and Predicted Power

5.6 Monthly and Annual Energy Generation (P_{out})

After generating a prediction model for calculating the power output ($\dot{P}_{out}$) in kilowatts, a conversion to kilojoules can be achieved by multiplying $\dot{P}_{out}$ by a time unit (kW=kJ/s). For example, in order to get the energy output (P_{out}) in kJ for one hour, $\dot{P}_{out}$ should be multiplied by 3600 seconds (1 hour = 3600 seconds). In this study, the monthly average energy generation is represented by a day in the middle of the month or specifically the 15th of each month, which means that this particular day represents an average for all days in a given month. A daily energy output in kJ can be calculated at the 15th of each month and then it can be multiplied by the number of days for that month to get the monthly energy output. Next, energy output for each of the 12 months can be summed to give the annual energy output of a SCPP for any given climate zone location in the U.S, as represented by a city in the climate zone containing the city.

Furthermore, detailed steps for calculating monthly energy outputs are provided in the next chapter.

5.7 Summary

An analytical model for calculating the power output of a SCPP was presented, with this analytical model using vertical velocities determined by the CFD analysis of a SCPP, which was presented in a previous chapter. Afterward, a prediction model for calculating power output was developed with the model consisting of a simplified polynomial equation that is a function of global horizontal irradiance and ambient temperature. This prediction model can then be used to find the annual and monthly energy generated by a SCPP for any set of environmental conditions, namely solar radiation and temperature.

6. SCPP SYSTEM ENERGY GENERATION FOR DIFFERENT U.S CLIMATE ZONES

6.1 Introduction

Until now, the focus has been on developing a model that can determine the power generation from a SCPP of fixed geometry and size, for any given set of environmental conditions to include solar irradiation and ambient temperature. The focus now shifts to applying the SCPP system model developed in this study to real-world applications, associated with geographical location and time of year. Specifically, this chapter evaluates SCPP power and energy output for different U.S climate zones and for different time-of-year periods, meaning month. In addition, SCPP energy outputs will be determined on monthly and annual basis and a comparison between these climate zones will be carried out. Furthermore, after completing these comparisons, a better understanding is achieved so that the applicability of the SCPP concept in the real world can be made.

6.2 Monthly Power and Energy Generation for Each Climate Zone

The power output prediction model, consisting of a polynomial equation that is a function of solar radiation and ambient temperature was formulated in Chapter 5, and it is used here to find the monthly average energy output, which is the energy output for a representative day and then the monthly total energy output for each of 12 months for each climate zone. Figure 6-1 provides detailed steps for calculating the monthly energy output in GJ. In addition, Table 6-1 shows a numerical example of using the process in Figure 6-1 to calculate the energy output for a specific month (January) and climate zone (CZ-2B). As a side note, the limits of the prediction model have been taken into account in the form of red highlighted values of GHI, that are considered to be out of the prediction model's limit, which is a region of low GHI and high temperature. An

important aspect of the Figure 6-1 process is that the averaged GHI_{Peak} is used in Step 5 in order to find the hourly GHI based on applying the sine wave assumption. Then, after getting the GHI for each hour, coupled with the daily average temperature for the representative month, the energy output (kJ) per day is calculated (Step 6 through Step 8) by first finding the power output for each hour, and then finding the energy output for each hour, which can then be summed to get a daily value. As discussed earlier, the 15^{th} of each month is used to represent a typical day for the month. Therefore, after calculating the energy output for day 15, this energy output can be multiplied by the number of days in the designated month to arrive at a total monthly energy output value, which is Step 9.

The above process has been applied to each climate zone for all 12 months, with Table 6-2 presenting monthly energy outputs for each case, which is arranged by climate zone and months.

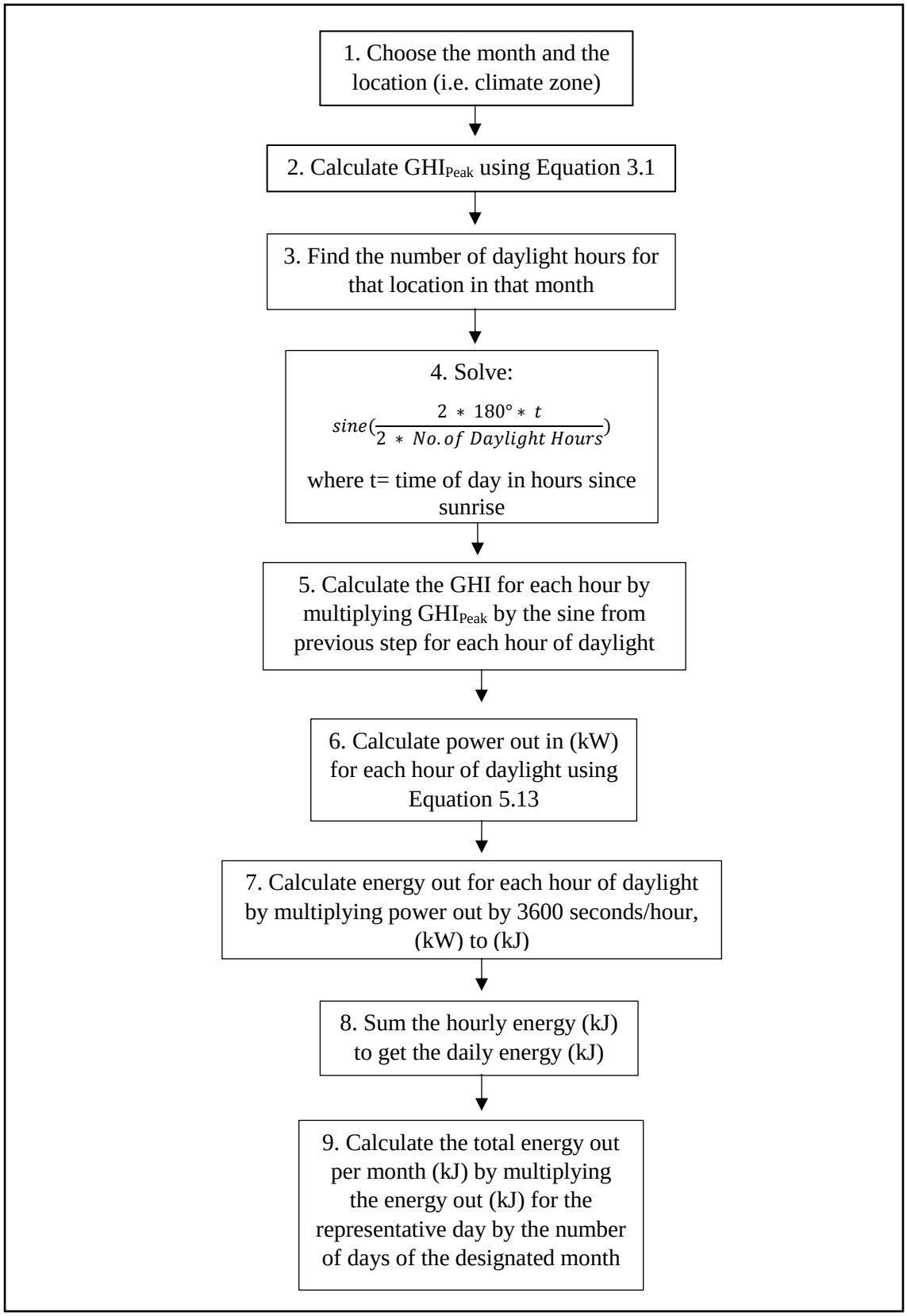

Figure 6-1 Steps for Calculating Monthly Energy Output in GJ for a Given Climate Zone Location

Table 6-1 Example of Calculated Monthly Energy Output for a Specific Climate Zone (CZ-2B)

			$A = \frac{2 * 180° * t}{2 * Length\ of\ Day}$									
		At the 15th										
Step 1	Step 2	Step 3		Step 4		Step 5	Step 6		Step 7	Step 8	Step 9	
Month	Avg. Peak GHI (W/m^2)	No. of Daylight Hours	Hour	A	Sin(A)	GHI	Avg. Temp. (°F)	Hourly Power (kW)	Hourly Energy (kJ)	Daily Energy (kJ)	No. of Days	Total Power Per Month (KJ)
January	549.03	10.18	1	17.68173	0.303729	166.76	57.5	0.00	0.00	454933.62	31	14,102,942.32
			2	35.36346	0.578761	317.76		7.94	28599.50			
			3	53.04519	0.79911	438.74		17.20	61904.96			
			4	70.72692	0.943956	518.26		23.28	83798.30			
			5	88.40864	0.999614	548.82		25.61	92210.97			
			6	106.0904	0.960826	527.52		23.99	86348.12			
			7	123.7721	0.831255	456.38		18.55	66763.69			
			8	141.4538	0.623145	342.13		9.81	35308.08			
			9	159.1356	0.356158	195.54		0.00	0.00			
			10	176.8173	0.05552	30.48		0.00	0.00			

Table 6-2 Monthly Energy Output for Different Climate Zones

	Total Energy Per Month (GJ)					
	1A	**2A**	**2B**	**3A-W**	**3A-E**	**3B-E**
January	13.3	9.4	14.1	11.9	10.9	13.4
February	15.6	11.6	17.7	14.4	15.1	17.1
March	22.4	18.5	24.7	22.0	23.3	27.0
April	26.9	22.8	37.0	29.5	30.7	36.1
May	25.2	24.1	41.6	32.5	29.9	35.4
June	25.0	25.8	41.9	35.7	28.6	37.8
July	27.9	29.8	37.6	33.7	26.4	32.8
August	22.8	21.2	34.9	30.0	27.2	30.9
September	19.9	21.2	29.2	22.6	22.6	22.4
October	15.5	17.6	21.4	20.6	17.4	21.5
November	11.7	11.9	15.4	11.4	12.2	13.1
December	11.6	8.4	11.1	9.9	9.5	12.5
Annual	237.8	222.4	326.7	274.2	253.8	300.1
	Total Energy Per Month (GJ)					
	3B-W	**3B-LV**	**3B-N**	**3C**	**4A**	**4B**
January	16.2	11.6	5.2	11.4	5.9	14.2
February	21.7	17.1	10.1	12.2	9.3	17.3
March	32.4	27.0	21.2	25.7	20.9	29.1
April	41.1	37.3	28.3	36.6	28.8	34.2
May	42.1	39.5	44.5	38.2	22.3	34.7
June	43.5	41.7	45.4	46.0	30.1	39.3
July	38.3	37.7	43.8	45.0	27.3	37.1
August	33.1	35.6	37.3	41.1	26.4	32.0
September	30.9	29.8	28.8	29.6	17.1	23.0
October	21.8	20.7	18.4	16.7	15.9	23.1

Table 6-2 Continued

	Total Energy Per Month (GJ)					
	3B-W	**3B-LV**	**3B-N**	**3C**	**4A**	**4B**
November	17.1	14.5	8.0	13.7	5.2	14.0
December	14.7	11.8	3.6	8.7	5.3	12.5
Annual	352.8	324.2	294.6	324.9	214.6	310.6
	Total Energy Per Month (GJ)					
	4C	**5A**	**5B**	**6A**	**6B**	**7A**
January	0.0	5.8	11.5	4.7	10.2	5.8
February	5.1	10.0	16.0	13.8	13.5	12.9
March	9.9	17.6	28.2	10.0	26.1	19.8
April	20.7	19.6	26.0	25.7	29.0	25.7
May	26.6	32.2	37.4	22.2	35.0	32.5
June	25.7	29.2	44.2	21.3	42.6	33.6
July	32.2	31.3	37.5	21.7	36.1	29.0
August	23.9	22.0	34.5	25.7	33.4	24.7
September	16.7	15.6	26.2	17.0	22.3	17.1
October	3.3	9.3	17.4	5.6	17.4	10.1
November	0.0	4.6	9.3	2.2	10.2	5.7
December	0.0	3.2	8.3	1.0	7.0	4.1
Annual	164.1	200.5	296.4	170.8	282.9	221.2

The values in Table 6-2 are plotted in Figure 6-2 to provide a comparison among different climate zones. In Figure 6-2, the x-axis represents the month of the year, while the y-axis represents the total energy output per month in GJ. Because Figure 6-2 is somewhat clutter making it difficult to reach conclusions regarding specific climate zones, the values of Table 6-2 is that overall trends can be spotted. For example, it can be seen in Figure 6-2 that the highest energy output for almost all climate zones occur during summer months, which is consistent with the fact that the GHI values during summer months are higher than any time of the year because of the sun being high in the sky or closer to the overhead in the summer. This behavior agrees with the results from the previous chapter where the power output was plotted against different

GHI values (Figure 5-1). Also, it should be noted that there is a higher solar energy input, and hence higher SCPP energy output, in the summer because daylight hours are longer compared to the winter.

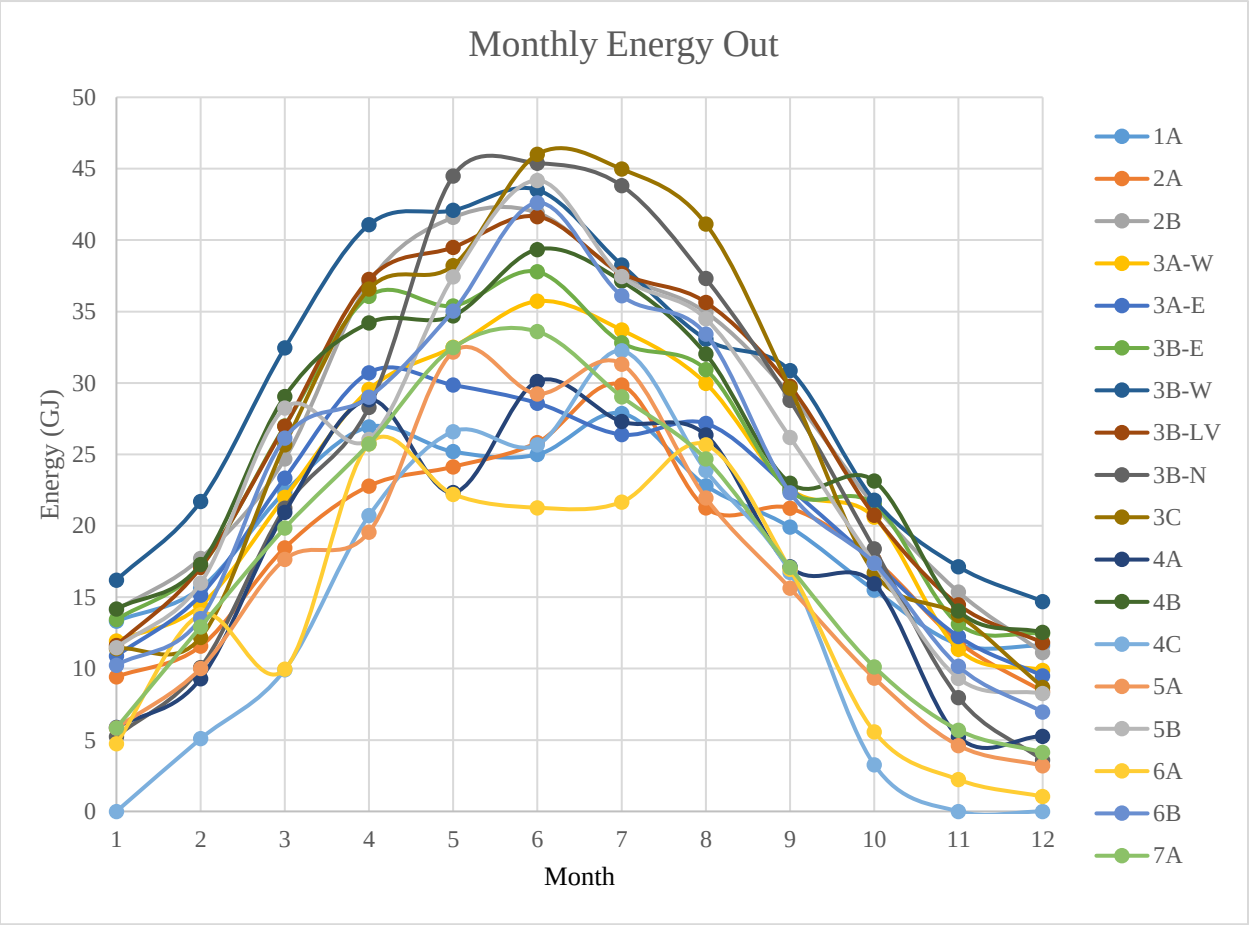

Figure 6-2 Illustration of Monthly Power Output for Different Climate Zones over a Course of the Year (area under curve is annual)

Additional comparisons are presented in Figure 6-3 through Figure 6-8 with these figures providing comparisons for common climate zones that fall under different categories. For example, results for climate zone 3, which is actually made of 7 subzones, including humid (A) and dry (B), are shown in Figure 6-3. It can observed that drier regions (B) output more energy

than humid regions (A), which is evident in the plots including Figure 6-4 through Figure 6-8. It can also been seen in Figure 6-3 that those subzones located in the west output more energy than those in the east. Figure 6-4 shows that marine climate namely 4C, have lower energy outputs.

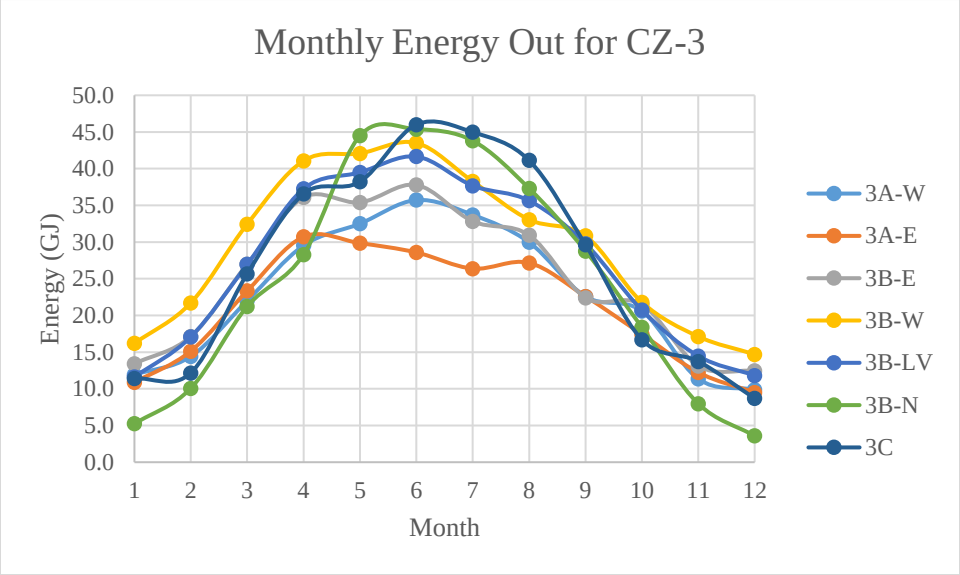

Figure 6-3 Monthly Energy output for Climate Zone 3 with Different humidity levels and locations

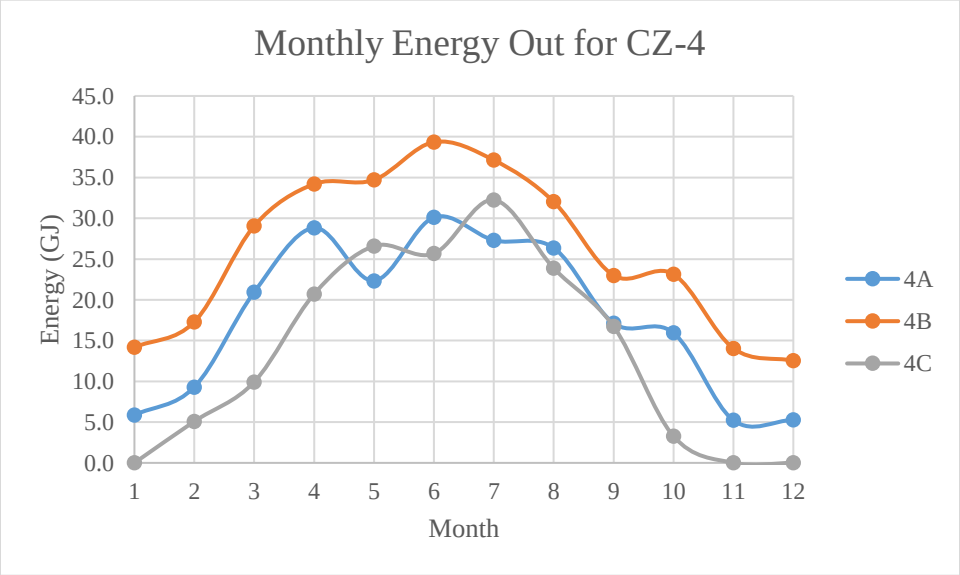

Figure 6-4 Monthly Energy output for Climate Zone 4 with Different humidity levels and locations

All humid (B) climate zones, are plotted in Figure 6-5 where the dry ones (A) are plotted in Figure 6-6. Comparing the two plots shows that differences are less pronounced in the winter months, while the energy output in summer months can be as much as 20% larger for drier regions (A).

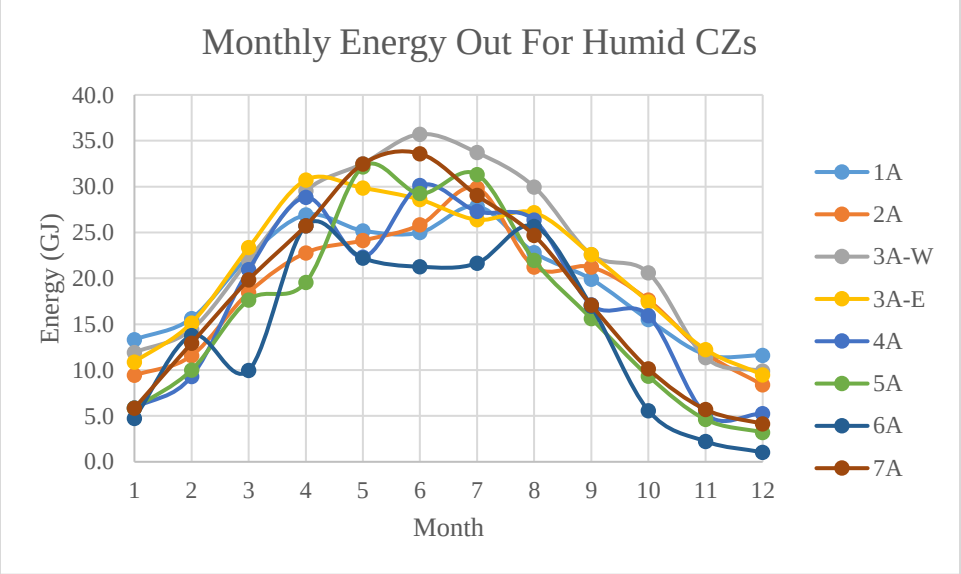

Figure 6-5 Monthly Energy output for Humid Climate Zones

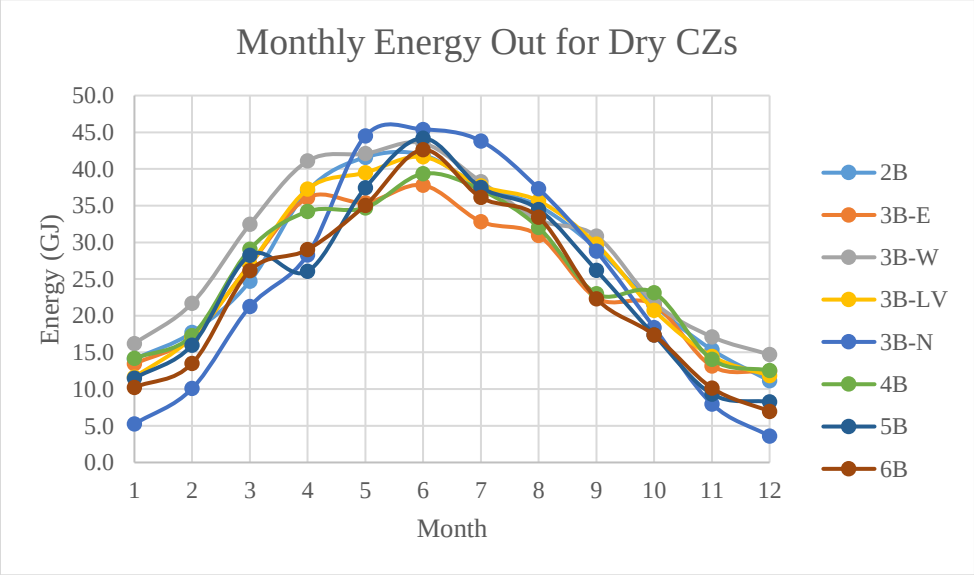

Figure 6-6 Monthly Energy output for Dry Climate Zones

The next two plots, compare results for the lowest numbered climate zones (hot regions), which are in Figure 6-7, and the highest numbered climate zones (cold regions), which are in Figure 6-8. As noted before, drier regions have greater monthly outputs especially in the summer, also shown is that the difference between hot and cold regions is not small in the summer, which may be the result of colder climates a larger latitude have longer days, which means that the SCPP can operate for more hours in the summer, with the opposite occurring in the winter.

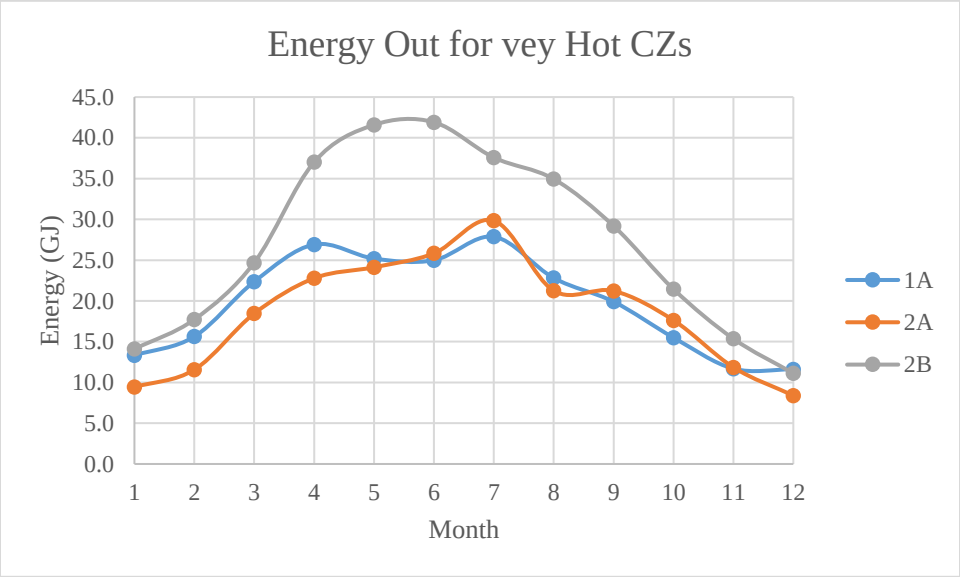

Figure 6-7 Monthly Energy output for Very Hot Climate Zones

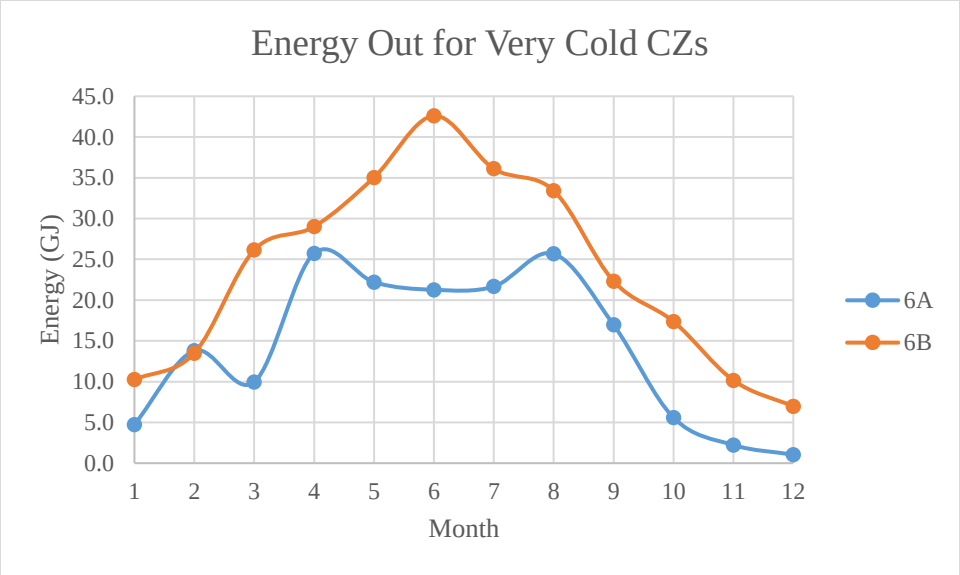

Figure 6-8 Monthly Energy output for Very Cold Climate Zones

6.3 Annual Energy Generation for Each Climate Zone

After getting the monthly energy output for each climate zone, the annual energy output can be found by simply adding the monthly energies for all twelve months of the year, again for each climate zone. Table 6-3 presents the annual energy output from a SCPP system for each of 18 climate zones. In addition, Figure 6-9 is a bar graph that compares annual energy outputs for all climate zones.

Table 6-3 Annual Energy Generation for Different Climate Zones

Climate Zone	Total Energy Per Year (GJ)
1A	237.8
2A	222.4
2B	326.7
3A-W	274.2
3A-E	253.8
3B-E	300.1
3B-W	352.8
3B-LV	324.2
3B-N	294.6
3C	324.9
4A	214.6
4B	310.6
4C	164.1
5A	200.5
5B	296.4
6A	170.8
6B	282.9
7A	221.2

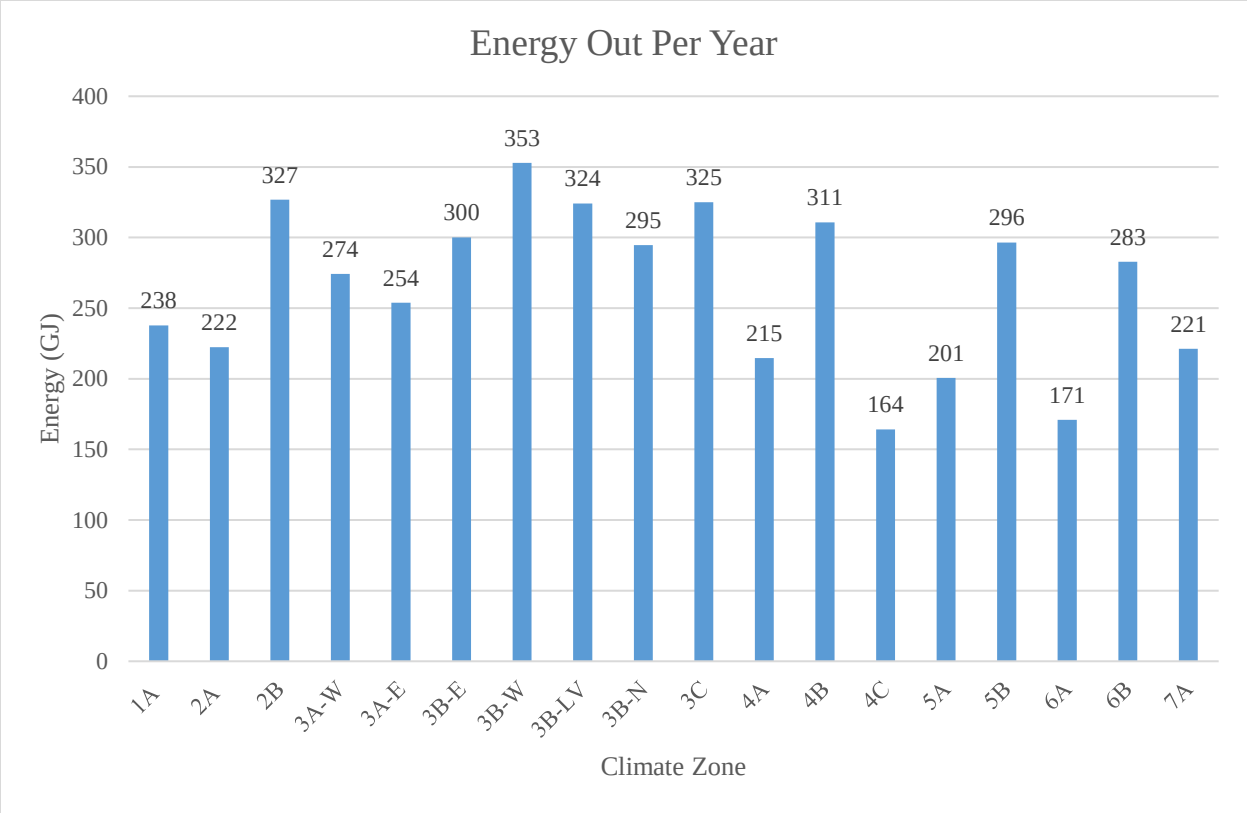

Figure 6-9 Annual Energy Output Comparison for Different Climate Zones

In Figure 6-9, different climate zones are represented on the x-axis, while the y-axis represents the annual energy generated in GJ. An interesting finding from Figure 6-9 is that the SCPP energy produced in climate zone 2A (222 GJ), which is represented by Houston, TX, almost matches the amount of energy produced in climate zone 7A (221 GJ), which is represented by Fargo, ND, although these two climate zones represent extreme temperature conditions of very hot to very cold, along with extreme latitudes with Houston being 29.76˚ and Fargo being 46.88˚. It is possible that this behavior is due to a combination of cloud cover, both are dry (A) but one could be drier than the other, and the result of the length of the day, for example, it is well known that the sun can shine for 24 hours at the summer solstice on the Arctic Circle (Grieser). From this observation, it can be surmised that the day length increases during summer months as one

moves from a Southern state (e.g., Texas) to a Northern state (e.g., North Dakota). The net result could mean that more solar energy strikes a unit area than one might think, even if the projected area is less at the higher latitude.

This length-of-day characteristic can be seen in Figure 6-10, which is a comparison of the total daylight hours for climate zones 2A and 7A for each month of the year. From this figure, one can see that the number of daylight hours in the northern part of the U.S is larger than the southern part for half the year during the Spring Equinox (March 21) to the Fall Equinox (September 21) period. On a side note, the results herein are represented by the 15^{th} (or center) of each month, which is slightly off from the 21^{st}, which is typically associated with the equinox and solstice. Based on the above observation of longer summer days in the northern part of the U.S, one can explain similar matches between the annual energy output values for climate zones 2A and 7A, even though the southern climate zones have GHI_{Peak} values that are higher than the northern climate zones as shown in Figure 6-11, which is a monthly comparison of GHI_{Peak} for climate zones 2A and 7A. As a final note, a plot of total daylight hours similar to Figure 6-10 for 2A and 7A is presented in Figure 6-12 to illustrate the behavior of each of 18 climate zones in the matter of number of daylight hours over a course of a year. Again one can see the longest number of summer daylight hours in northern climate zones.

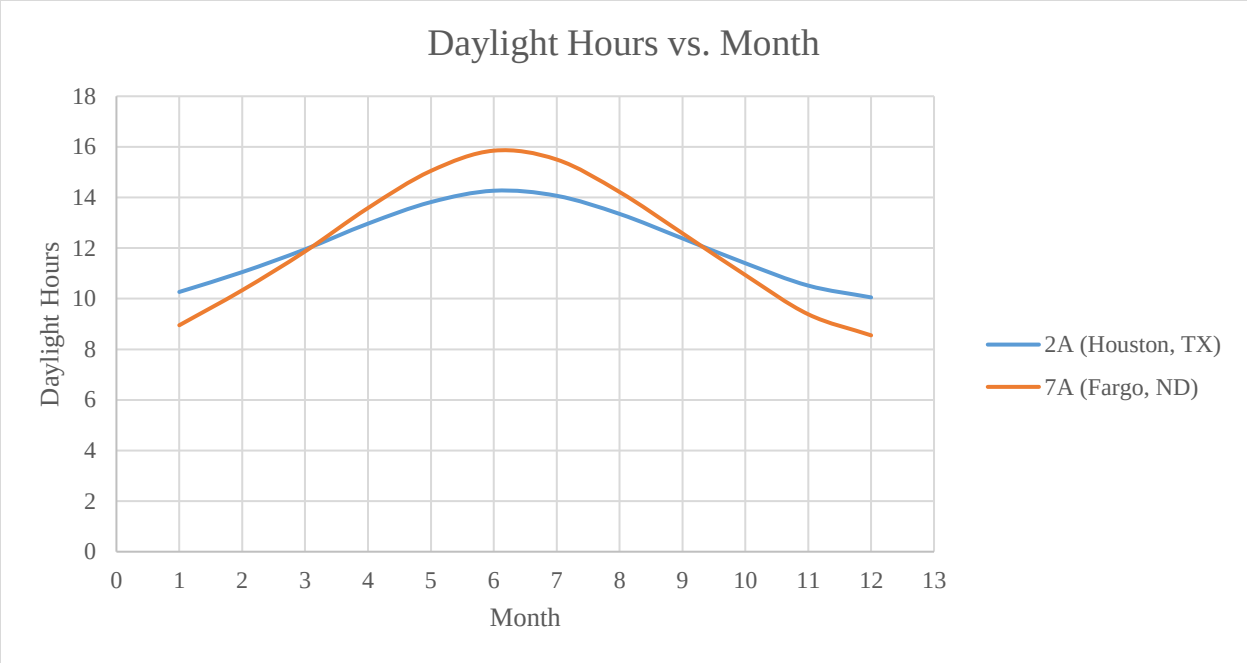

Figure 6-10 Comparison of Day Length for two Different Climate Zones

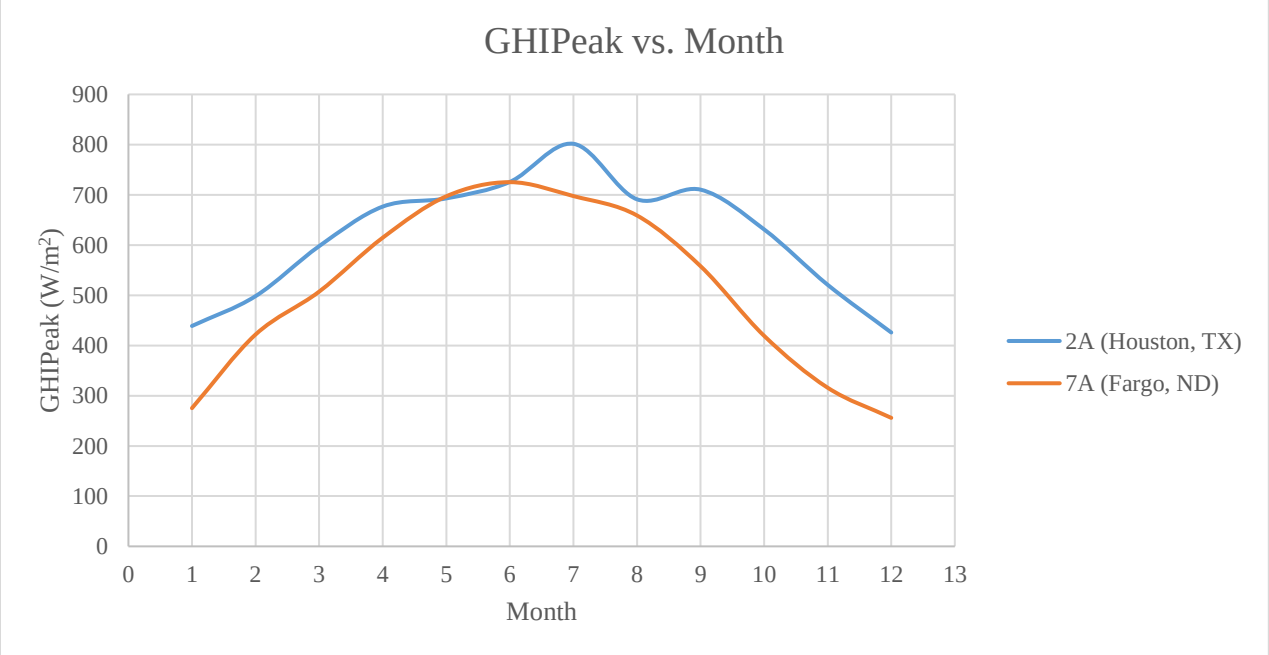

Figure 6-11 Comparison of GHI_{Peak} Values for two Different Climate Zones

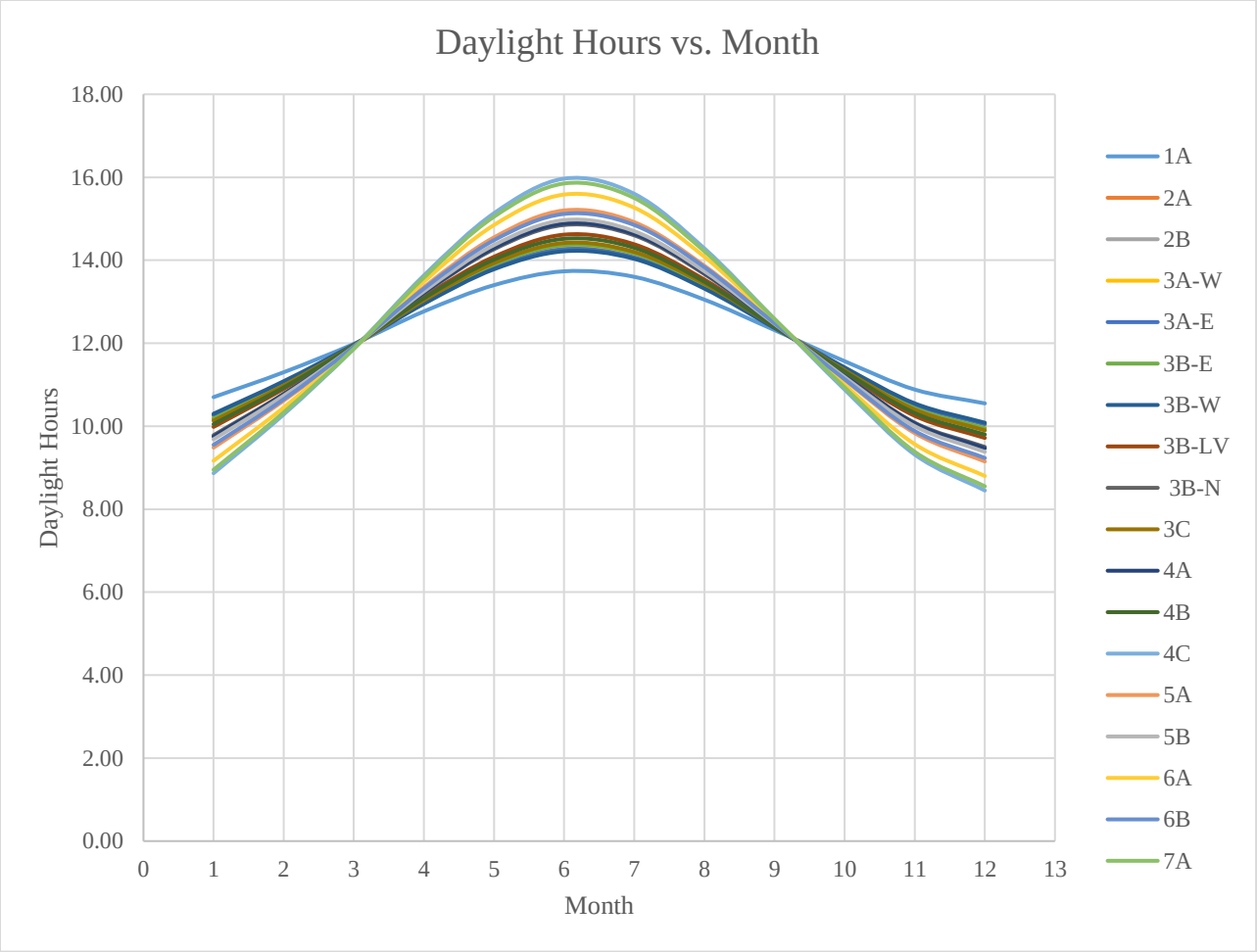

Figure 6-12 Number of Daylight Hours vs. Month for Different Climate Zones

6.4 Annual Daylight Hours

The annual energy output of each climate zone can be further investigated in term of latitude angle and annual daylight hours. Table 6-4 presents the latitude angles, annual daylight hours and annual energy outputs from the SCPP for all 18 climate zones along with their representative cities. A side note here is that the annual daylight hours were calculated based on the daylight hours that occur on the 15th of each month. An interesting observation from Table 6-4 is that the total annual daylight hours is somewhat independent of latitude, being around 4450 hours.

Figure 6-13 presents the annual energy produced by a SCPP versus the latitude angle for all 18 climate zones. The annual energy output versus latitude behavior shown in Figure 6-13 is somewhat mixed in that the mid-latitude from about 33˚to 42˚ appears to have the largest energy outputs with the extreme of small and large latitudes being less, which is where Houston and Fargo occur. Even with that said, it appears that the large latitude climate zones produce less annual energy than small latitude climate zones, which would seem to indicate that other reasons need be taken into account to explain the equivalence of Houston and Fargo such as cloud cover and humidity.

In addition, the annual energy output of a SCPP against the annual daylight hours is illustrated in Figure 6-14 for all 18 climate zones. The number of daylight hours fall in a narrow range of about 4437 to 4471 but even so it would appear that the larger latitude with the larger number of daylight hours produce less annual energy, which is probably due to the GHI's being smaller at larger latitude.

Finally, the annual daylight hours versus the altitude angles for all 18 climate zones is plotted in Figure 6-15. The number of annual daylight hours slightly increases as the latitude increases; however, this increase from 4445 to 4470 hours is less than 1%, being only 0.6%.

Table 6-4 Latitude, Annual Daylight Hours and Annual Energy Output for all Climate Zones

Climate Zone	City, State	Latitude (˚)	Annual Daylight Hours	Total Energy output per Year (GJ)
1A	Miami, FL	25.76	4445	238
2A	Houston, TX	29.76	4438	222
3B-W	El Paso, TX	31.77	4445	353
3A-E	Montgomery, AL	32.38	4445	254
3A-W	Dallas, TX	32.78	4445	274
2B	Phoenix, AZ	33.45	4446	327
3B-E	Lubbock, TX	33.58	4446	300
3C	Santa Monica, CA	34.02	4447	325
4B	Amarillo, TX	35.22	4448	311
3B-LV	Las Vegas, NV	36.17	4450	324
3B-N	Sacramento, CA	38.58	4453	295
5B	Denver, CO	39.74	4455	296
6B	Cheyenne, WY	41.14	4457	283
5A	Chicago, IL	41.88	4458	201
6A	St. Paul, MN	44.95	4465	171
7A	Fargo, ND	46.88	4468	221
4C	Seattle, WA	47.61	4471	164
4A	Washington DC	47.75	4454	215

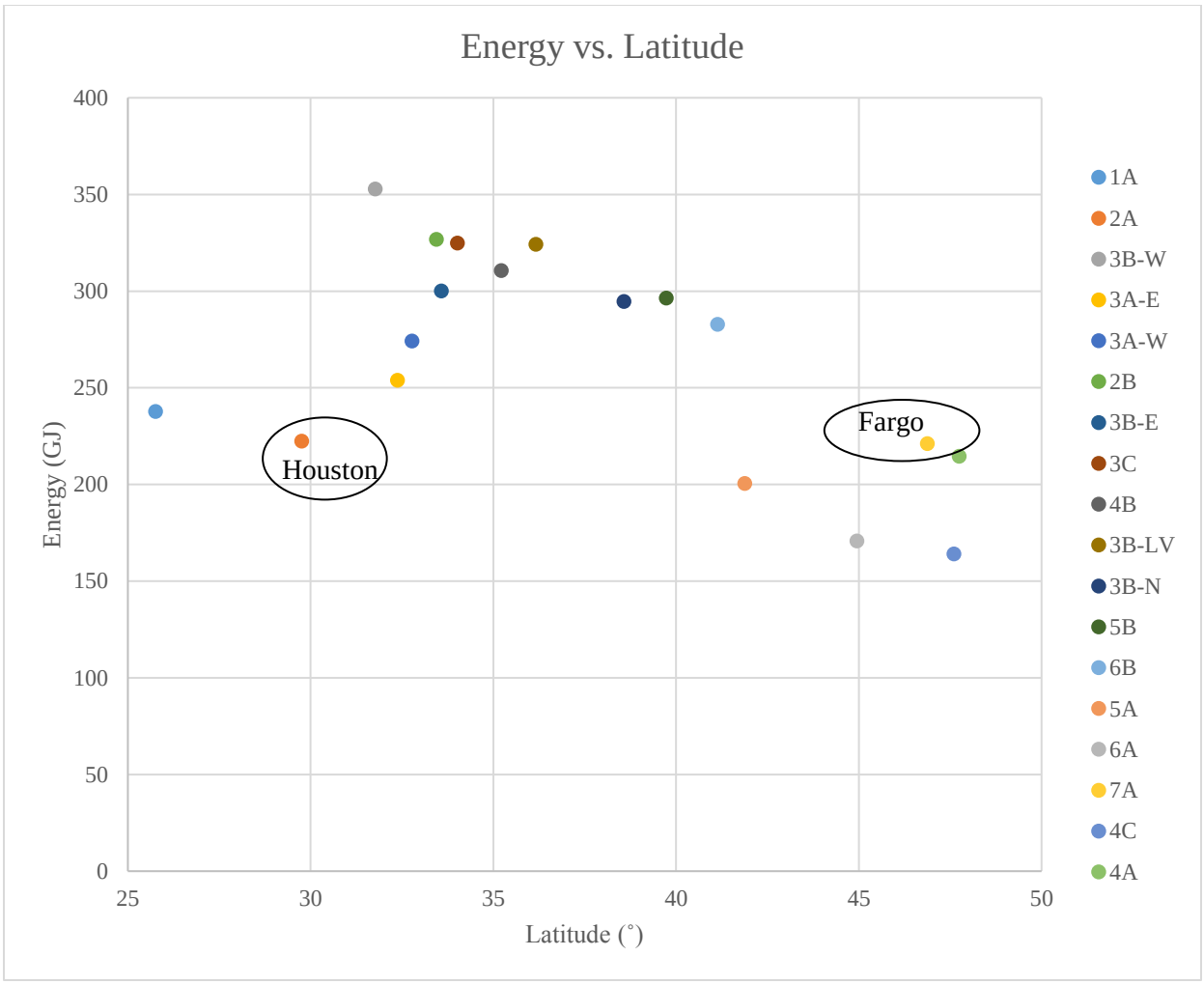

Figure 6-13 Annual Energy output vs. Latitude for all climate zones

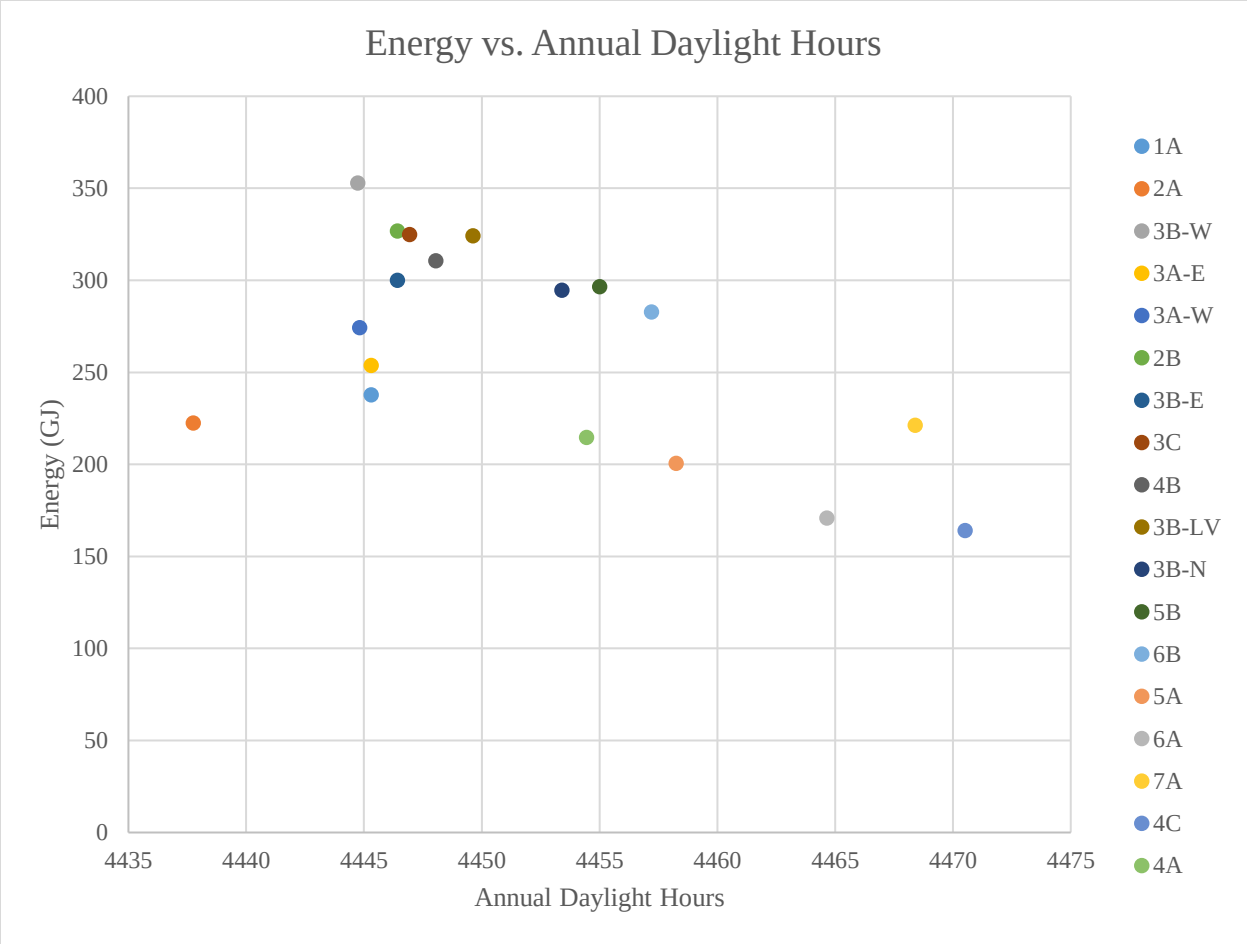

Figure 6-14 Annual Energy output vs. Annual Daylight Hours for all climate zones

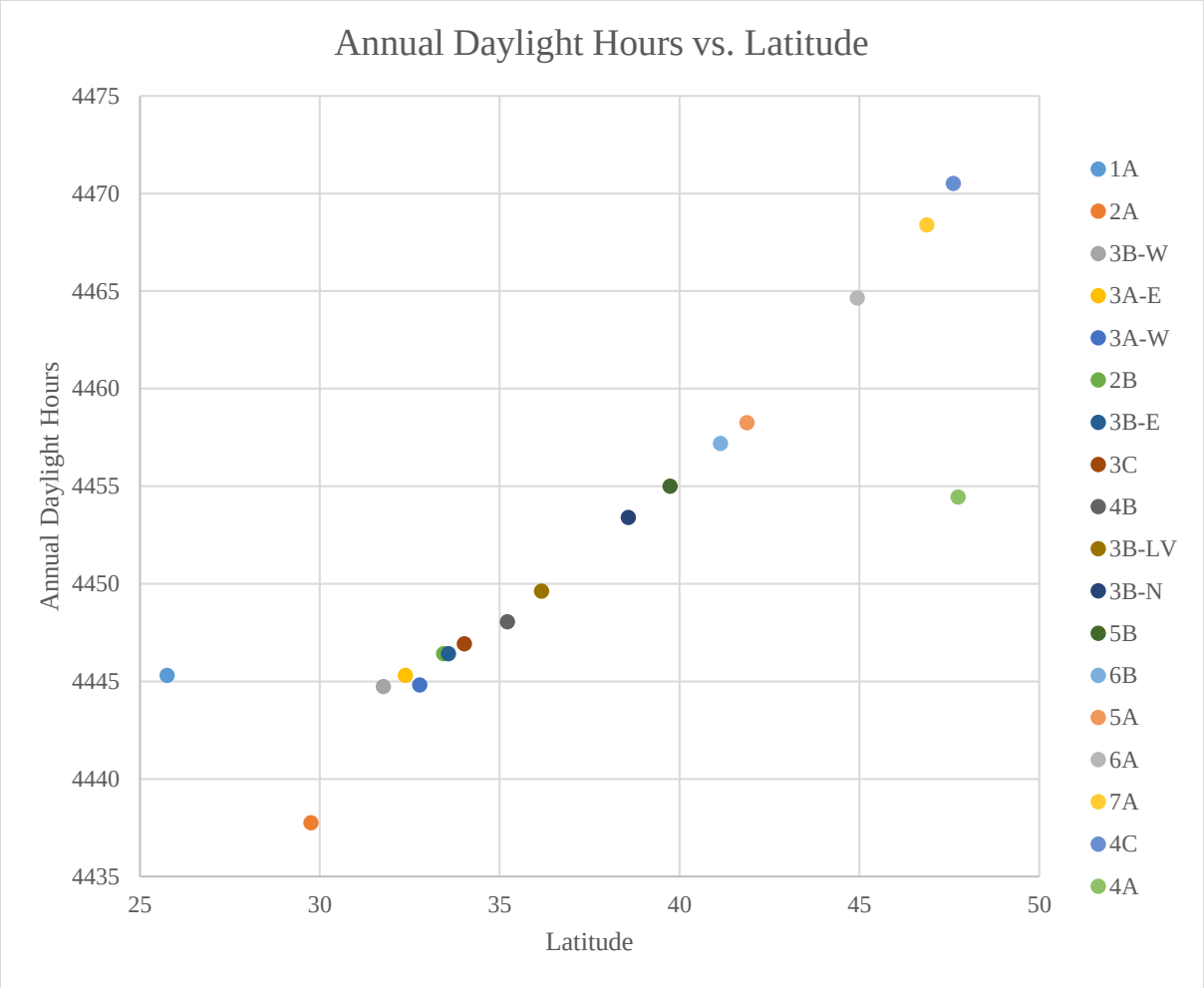

Figure 6-15 Annual Daylight Hours vs. Latitude for all Climate Zones

7. CONCLUSION

7.1 Summary

The Solar Chimney Power Plant (SCPP) concept was investigated by a combination of modeling and analysis with a focus on determining output power as a function of geometry, size and most importantly environmental conditions, such as solar radiation and ambient temperature, which were varied over the full range of real-world values. A literature review was performed in order to find and evaluate both the historical developments of the SCPP concept and the most recent research performed since 2016, with the latter providing the foundation for the present research. Specifically, the SCPP concept used in a Spanish prototype study was initially followed herein by building a similar solar model, which included a unique CFD analysis. A comparison with the Spanish prototype output was then performed to verify the SCPP solar model's validity, prior to expanding and upgrading it for this study. After building, validating and upgrading the SCPP solar model, so that its useful output would be the maximum chimney velocity, the working concept of the SCPP was applied to 18 different regions in the U.S with each region being associated with a different climate zone.

Before applying the SCPP concept to the 18 different climate zones, which cover all of the U.S, a number of additional modeling steps were performed. First, the validated SCPP solar model was used to generate a large velocity data file for several different input parameters. Specifically, these generated data files resulted in velocity values at the bottom of the SCPP chimney as functions of solar irradiance and ambient temperature, which are the main contributors to the air movement inside the SCPP, especially since the geometry and size are fixed for this study.

In order to apply the SCPP concept to the real world of different geographical regions, it was necessary to develop prediction equations for the two main power contributors, namely solar

irradiance and ambient temperature, which are both functions of time of year and climate zone. These two prediction equations are eventually polynomial equations that are solved by using a statistics package that takes time of year and climate zone environmental data files and solved for the polynomial coefficients. The two prediction equations then used to calculate environmental parameters for any time of year and for any location or climate zone.

To complete the SCPP modeling effort, it was necessary to develop an analytical model for calculating the power output of a SCPP based on knowing the velocity at the bottom of chimney. The data generated from the CFD model, specifically the velocity, were then used to generate a power output for each velocity, which means that power output is a function of solar irradiance and ambient temperature. Finally, an output power prediction model, was developed by solving a polynomial equation with the aid of a statistics package, so that one can calculate the power output of a SCPP as a function of solar irradiance and ambient temperature.

The SCPP power prediction model, consisting of several prediction equations described above, was applied to different climate zones in the U.S on a monthly basis, and a comparison was carried out. First, it was shown that the energy production for all 18 different climate zones increased during summer months, while decreasing during winter months. Furthermore, climate zone 3B-W, which is represented by El Paso, TX, produced the highest annual energy output of around 352 GJ. On the other hand, the lowest amount of energy generated of 164 GJ was in climate zone 4C, which is represented by Seattle, WA.

Ultimately, many of the climate zones produced similar magnitudes of annual SCPP energy, which was somewhat surprising considering the diverse range of latitudes represented by the various climate zones. At first glance, one might think that larger latitudes in the North would produce lower energies; however, this was not the case, possibly, because the length of the day,

which is an important factor that affects power output, changes with latitude. For example, at the summer solstice the length of the day increases as the latitude increases, which means that northern regions in the U.S may produce more energy in the summer compared to southern regions, which could explain some similarities in the amount of energy generated from two different diverse climate zones, namely Houston, TX with 222 GJ and Fargo, ND with 221 GJ. Two additional factors that could explain the above, with one reason being significant difference in cloud cover and/or humidity, which could affect GHI, regardless of the latitude. The second possible reason is that the lower temperatures associated with northern regions could produce larger SCPP energies, which were shown herein to increase as temperature decreased.

7.2 Future Work

In the future, a SCPP annual energy production analysis will be performed based on using units converted into kW.hr. This analysis will focus on comparing the SCPP output with other power production techniques especially those related to alternative energy, and at the same time it will facilitate an economic study for applying the SCPP concept in the U.S.

The accuracy of the prediction models generated in this study can be improved. Specifically, more cities can be added for each climate zone in order to increase the number of GHI data points for each climate zone, which in turn will improve the prediction model accuracy.

This study was based on using one SCPP geometry and size, which is based on the Spanish prototype. A follow up study would be focus on expanding the model so as to be able to input tower heights and diameters, also with collector height and area (i.e. diameter). As a result energy outputs can be calculated for a range of sizes and optimization studies can be performed.

Comparing energy outputs for different climate zones showed that there are possible functional relationships among energy output, number of daylight hours, latitudes, and possibly cloud cover and/or humidity, with the latter certainly affecting GHI. Follow up studies that include a larger data sets and possibly additional weather parameters could provide additional understanding of SCPP operations,

REFERENCES

ANSYS-FLUENT. "Ansys-Fluent.", https://www.ansys.com/products/fluids/ansys-fluent.

Ayadi, Ahmed, Abdallah Bouabidi, Zied Driss, and Mohamed Salah Abid. 2018. "Experimental and Numerical Analysis of the Collector Roof Height Effect on the Solar Chimney Performance." *Renewable Energy* 115: 649-662. doi:10.1016/j.renene.2017.08.099. https://www.sciencedirect.com/science/article/pii/S0960148117308583.

Cabanyes, I. 1903. "Las Chimeneas Solares (Solar Chimneys)." *La Ernergia Eléctrica*.

Grieser, Justin. "The Washington Post.", https://www.washingtonpost.com/news/capital-weather-gang/wp/2013/06/20/summer-solstice-2013-northern-hemispheres-longest-day-highest-sun-of-the-year/?utm_term=.dcc8a68d08d3.

Haaf, W., K. Friedrich, G. Mayr, and J. Schlaich. 1983. "Solar Chimneys Part I: Principle and Construction of the Pilot Plant in Manzanares." *International Journal of Solar Energy* 2 (1): 3-20.

Hassan, Aakash, Majid Ali, and Adeel Waqas. 2018. "Numerical Investigation on Performance of Solar Chimney Power Plant by Varying Collector Slope and Chimney Diverging Angle." *Energy* 142: 411-425. doi:10.1016/j.energy.2017.10.047. https://www.sciencedirect.com/science/article/pii/S0360544217317164.

Hu, Siyang, Dennis Y. C. Leung, and John C. Y. Chan. 2017. "Impact of the Geometry of Divergent Chimneys on the Power Output of a Solar Chimney Power Plant." *Energy* 120: 1-11. doi:10.1016/j.energy.2016.12.098. https://www.sciencedirect.com/science/article/pii/S0360544216319041.

Huang, Ming-Hua, Lei Chen, Ya-Ling He, Jun-Ji Cao, and Wen-Quan Tao. 2017. "A Two-Dimensional Simulation Method of the Solar Chimney Power Plant with a New Radiation Model for the Collector." *International Communications in Heat and Mass Transfer* 85: 100-106. doi:10.1016/j.icheatmasstransfer.2017.04.014. https://www.sciencedirect.com/science/article/pii/S0735193317300830.

Incropera, Frank P., David P. Dewitt, Theodore L. Bergman, and Adrienne S. Lavine. 2007. *Fundamentals of Heat and Mass Transfer*. Sixth ed. John Wiley & Sons.

Milani Shirvan, Kamel, Soroush Mirzakhanlari, Mojtaba Mamourian, and Nidal Abu-Hamdeh. 2017. "Numerical Investigation and Sensitivity Analysis of Effective Parameters to Obtain Potential Maximum Power Output: A Case Study on Zanjan Prototype Solar Chimney Power Plant." *Energy Conversion and Management* 136: 350-360. doi:10.1016/j.enconman.2016.12.081. https://www.sciencedirect.com/science/article/pii/S0196890416311761.

Najm, Omar A. and S. Shaaban. 2018. "Numerical Investigation and Optimization of the Solar Chimney Collector Performance and Power Density." *Energy Conversion and Management* 168: 150-161. doi:10.1016/j.enconman.2018.04.089. https://www.sciencedirect.com/science/article/pii/S0196890418304370.

NREL. "Tmy3.", https://rredc.nrel.gov/solar/old_data/nsrdb/1991-2005/tmy3/.

Rabehi, Rayan, Abla Chaker, Tingzhen Ming, and Tingrui Gong. 2018. "Numerical Simulation of Solar Chimney Power Plant Adopting the Fan Model." *Renewable Energy* 126: 1093-1101. doi:10.1016/j.renene.2018.04.016. https://www.sciencedirect.com/science/article/pii/S0960148118304221.

Schlaich, J. 1995. *The Solar Chimney: Electricity from the Sun* Edition Axel Menges.

Stockinger, Christopher. 2016. "Numerical Analysis of Airflow and Output of Solar Chimney Power Plants "Virginia Polytechnic Institute and State University.

Xu, Guoliang, Tingzhen Ming, Yuan Pan, Fanlong Meng, and Cheng Zhou. 2011. "Numerical Analysis on the Performance of Solar Chimney Power Plant System." *Energy Conversion and Management* 52 (2): 876-883.